Fluorescence Correlation Spectroscopy in Space and Time

Daniel Y. K. Aik and Thorsten Wohland

Contents

Abstract Fluorescence Correlation Spectroscopy (FCS) is a widely used technique to determine molecular dynamics and interactions. It uses observation volumes on the order of a femtolitre in size to distinguish the signal from single molecules against the background. As it is difficult to illuminate and specifically detect signals from such a small observation volume, FCS was originally conceived as a

D. Y. K. Aik
Department of Chemistry, National University of Singapore, Singapore, Singapore

Center for BioImaging Sciences, National University of Singapore, Singapore, Singapore

T. Wohland (✉)
Department of Chemistry, National University of Singapore, Singapore, Singapore

Center for BioImaging Sciences, National University of Singapore, Singapore, Singapore

Department of Biological Sciences, National University of Singapore, Singapore, Singapore
e-mail: twohland@nus.edu.sg

R. Šachl, M. Amaro (eds.), *Fluorescence Spectroscopy and Microscopy in Biology*,
Springer Ser Fluoresc (2023) 20: 233–274, https://doi.org/10.1007/4243_2022_36,
Published online: 27 November 2022

single-spot measurement that measures mainly temporal information. Multiplexing was then achieved by sequential scanning and detecting different spots in a sample and thus also providing spatial information. With advances in technology, the introduction of different illumination and detection methods, and the emergence of super-resolution and light-sheet microscopy, new opportunities opened up to collect thousands of contiguous spots in a sample and thus provide high-resolution spatio-temporal information over a whole cross-section of a sample. This chapter describes the different 2D FCS modalities, their advantages and disadvantages, and some of their applications.

Keyword Fluorescence correlation spectroscopy · Image correlation spectroscopy · Imaging FCS · Scanning FCS

1 Introduction

Fluorescence Correlation Spectroscopy (FCS) combines various principles and concepts to provide a powerful technique to gain insights into molecular processes [1, 2]. First, as the name indicates, FCS is based on fluorescence, a technique that provides multiple advantages. A fluorophore excited in a particular wavelength range, determined by its excitation spectrum, will generally emit at a longer wavelength, defined by its emission spectrum. This shift in wavelength, the so-called Stokes shift, allows easy distinction of the fluorescence from the excitation wavelength. It is this property, in combination with its high absorption cross-section and quantum yield, that results in a signal-to-noise ratio in fluorescence measurements that allows detection of a single molecule against the scattering background of other processes. Furthermore, fluorescence is linear over a very wide concentration range, up to mM, covering most physiological relevant concentrations of biomolecules, making quantification simple. And by using fluorescent labels to tag molecules of interest, it is specific and selective in its observations.

The second concept is the concept of fluctuations, i.e. the deviation of the signal from its mean value. Fluctuations of system-characteristic molecular processes in an equilibrium system are driven by thermal energy. These molecular processes, in turn, can be analysed in detail by the properties of the fluctuations. The importance of this concept is sometimes reflected in the overarching name of Fluorescence Fluctuation Spectroscopy (FFS), which denotes all fluorescence modalities that are based on the measurement and analysis of fluorescence fluctuations, including FCS and many derived modalities.

Lastly, correlations are a statistical analysis tool that is used to extract information from the measured fluorescence fluctuations. Suppose one has an understanding of the fluctuation-creating process and its parameters. In that case, this can be combined with the mode of fluorescence excitation and detection to create theoretical models for the expected correlation functions. These theoretical models can be fitted to

experimental data to extract values for the characteristic parameters. Although any process that can influence the fluctuations can be investigated by FCS, including chemical reactions, photophysical processes, rotation, and more, it mainly measures translational diffusion. Translational diffusion creates fluctuations by particles moving in and out of an observation volume. The correlation analysis can extract the diffusion coefficient and the average number of particles in the observation volume.

FCS was originally conceived as a single-point time trace measurement but was soon afterwards extended to spatial and spatiotemporal correlations. This extension was pursued along three interrelated paths. First, the concept of FCS, which measures temporal correlations at a single point, was transferred to spatial correlations within fluorescence images in Imaging Correlation Spectroscopy (ICS) [3]. ICS has no intrinsic time resolution and reports on spatial patterns that allow counting particles and determining particle cluster's sizes. Time resolution in ICS can be added by acquiring multiple images, with the time resolution being limited by the available image acquisition time. This was first achieved in temporal ICS, or TICS [4]. TICS is a compelling approach and was the first to be extended to spatiotemporal correlations for whole images in the form of Spatiotemporal ICS (STICS) [5] and other related techniques, as will be discussed in later sections.

The second approach was based on laser scanning. Flow influences the correlation function as it changes the way and the duration of particles moving through the observation volume [6]. As flow is in principle indistinguishable from a steady laser movement, the same correlation function applied to scanning FCS in which the laser beam is scanned through the sample at a constant speed [3, 7–10].

In scanning approaches, the confocal volume was moved at a particular speed and path through the sample. Although this required the use of more complex correlation functions, it provided several advantages. First, FCS is inherently only able to measure a process if fluctuations are created. In the classical approach, slowly moving or immobile particles cannot be observed when diffusion is measured, leaving crucial molecules in a sample inaccessible. By scanning the confocal volume, even stationary particles will contribute to the correlation function when the confocal volume is scanned over them, leading to characteristic fluctuations related to the scan speed instead of the diffusion coefficient [6]. Mobile particles still contribute to the correlation function with their processes now dependent on diffusion coefficient and scan speed. Second, scanning breaks the symmetry of the correlation function as the scanning process defines a direction within the sample. This is useful in the case that the process under study itself has a privileged direction. The classic example, in this case, is flow or active transport of particles.

In the case of flow, the autocorrelation function (ACF) derived from a stationary confocal volume will show the changing dynamics but cannot determine the flow direction. In contrast, scanning FCS will lead to different correlation functions depending on whether one scans along, against, or at an angle to the flow direction [11, 12]. It can thus determine flow velocities and profiles. Finally, the inherent time resolution in scanning, specified by the time the confocal detection dwells on a single pixel, is much higher than can be reached in the acquisition of whole images, as done

in other spatiotemporal correlation techniques and thus can detect even very fast events.

To access the spatial information, one needs to know the position of the laser beam at each time point, i.e. the scan path needs to be known precisely. Scanning allows calculating correlations for each point of the laser trajectory. Koppel et al. used a confocal microscope to determine molecular mobility in solution and bilayers in so-called Scanning Concentration Correlation Spectroscopy (SCCS) [13]. In Position-Sensitive Scanning FCS (PSFCS), a circular trajectory was used to determine flow directions [14]. Using the inherent time structure in confocal images, Raster Image Correlation Spectroscopy (RICS) finally allowed to access molecular mobility in a whole image [15].

The third path was based on FCS multiplexing by collecting multiple temporal correlation functions simultaneously. Brinkmeier et al. used two-beam cross-correlation analysis to measure flow in microstructures [16, 17], which was subsequently extended to two-photon excitation [18]. A similar idea was implemented by detecting different parts of one single confocal volume, either using two pinholes [19] or using one pinhole but shifting the detectors with respect to the pinhole instead [20]. This was further optimized with modern instruments that use multi-element or multipoint detectors [21, 22].

Here also the advantage of combining temporal and spatial correlation functions was immediately recognized. A single-point measurement was able to determine flow speeds but could not determine the direction of flow, necessary for the determination of flow velocities and flow profiles. In the case of two points, however, the forward and backward correlation functions provide a means to determine flow directions and thus to measure flow profiles. Another advantage of multipoint FCS was that the distance between the points could be precisely controlled and thus was known. Since cross-correlations between the points provided information on how long particles needed to move from one point to the other and the distance between the points was known, the measurements required no calibration.

The measurements could be made so precise that even sub-nanometre differences in hydrodynamic radius could be measured by the so-called dual-focus FCS [23–25]. The extension to more points was first achieved only with a small number of points by either using multiple single-point detectors [26, 27] or using small multipixel devices that could be read out sufficiently fast to measure molecular dynamics in biological samples [26, 28].

This situation changed when it was shown that electron-multiplying charged-coupled device (EMCCD) and scientific complementary metal-oxide semiconductor (sCMOS) cameras could be read out sufficiently fast, at least for regions of interest on the order of 100–1,000 pixels [29–33]. Since then, the so-called Imaging FCS approaches have allowed the temporal correlation function for each pixel or the spatiotemporal correlation functions between any pixels or group of pixels to be calculated. Imaging FCS has been developed and applied to a wide range of samples, from solution measurements to cells and organisms [34, 35].

The three approaches thus resulted in methods to measure molecular spatiotemporal dynamics over whole images with different advantages and disadvantages as will be discussed in this chapter.

2 Image-Based Correlation Spectroscopy

Image Correlation Spectroscopy (ICS) is the spatial analogue to FCS. While FCS analyses patterns in time, which are interpreted as the dynamics of molecular processes, ICS analyses patterns in space in images or series of images (Fig. 1a) to

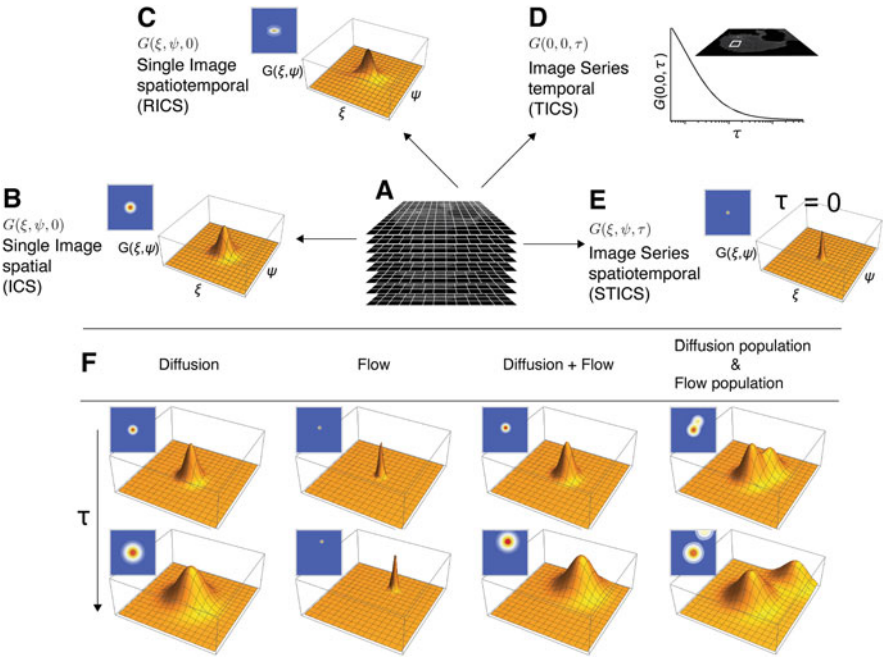

Fig. 1 Image-based correlation spectroscopy. (**a**) A single image or a time stack of images is recorded. (**b**) Single images can provide spatial resolution in ICS, providing data on the number of particles and cluster sizes. (**c**) If the image was scanned and contained inherent time resolution, it could be used in RICS to extract the number of particles at each ROI and spatiotemporal information, including diffusion coefficients, flow parameters, and binding interactions. (**d**) In a stack of frames, the temporal information can be extracted for each ROI in an image. (**e**) And in STICS the spatial and temporal information of the image stack is recovered. (**f**) Examples of processes in STICS: diffusion broadens the central peak of the correlation function; flow moves the peak with time; diffusion and flow of a single component shows a combination of correlation peak movement and broadening; and if there are two components, one diffusing and the other undergoing flow, then two correlation peaks will develop a broadening central peak and a second peak that broadens and moves away from the origin

yield information on numbers and sizes of structures. The combination of time and spatial correlation analysis leads to the general equation for the correlation function.

$$G_{ab}(\xi, \psi, \tau) = \frac{\left\langle \langle \delta I_a(x, \ y, \ t) \delta I_b(x+\xi, \ y+\psi, \ t+\tau) \rangle_{xy} \right\rangle_t}{\langle I_a \rangle_t \langle I_b \rangle_{t+\tau}} \tag{1}$$

Here $\delta I_a(x, y, t)$ is the intensity fluctuation in wavelength channel a at a particular position (x, y) at time t. $\delta I_b(x + \xi, y + \psi, t + \tau)$ is the intensity fluctuation in wavelength channel b at a particular position and time shifted by (ξ, ψ, τ) compared to $\delta I_a(x, y, t)$. The values (ξ, ψ, τ) are often called the spatial and temporal lags of the correlation. The angular brackets $\langle \ldots \rangle_p$ indicate averaging with respect to the parameter p. The indices a and b stand for different wavelength channels when performing dual colour-cross-correlation spectroscopy, for auto correlation analysis they can be omitted. This equation will be adapted in multiple ways, leading to various 2D FCS methods that emphasize the correlations' spatial, temporal, or spatiotemporal aspects. In principle, any imaging technique can provide data for these methods, including confocal scanning laser microscopy (CLSM), spinning disk confocal microscopy (SDCM), total internal reflection fluorescence microscopy (TIRFM), or light-sheet microscopy (LSM).

All these microscopy techniques contain, in principle, spatial and temporal information as images can either be collected as a time series, or in the case of CLSM, have an inherent time structure as pixels in the image are collected sequentially. However, the exploitation of the temporal information is only possible if the acquisition times are faster than the molecular processes to be observed. This section reviews different versions of ICS and how it expanded over time to arrive at spatiotemporal ICS (STICS), which fully analyses spatiotemporal information.

2.1 Image Correlation Spectroscopy: ICS

In the following, we write the correlation function again in the most general form with the indices a and b presenting images taken of the same sample in two different wavelength ranges. For $a = b$, we have an autocorrelation for ICS proper (Fig. 1b). If $a \neq b$, we speak of Image Cross-Correlation Spectroscopy (ICCS). ICS/ICCS takes input images and analyses them only in the spatial domain. Thus, the general function has no time component and takes the form

$$G_{ab}(\xi, \psi, 0) = \frac{\langle \delta I_a(x, \ y, \ t) \delta I_b(x+\xi, \ y+\psi, \ t) \rangle}{\langle I_a(t) \rangle \langle I_b(t) \rangle} \tag{2}$$

In this case, the correlation function can be calculated over the 2D Fourier Transforms (FT) of the image(s)

$$G_{ab}(\xi, \psi, 0) = FT^{-1}\{FT[Image_a] \times FT[Image_b]\} \tag{3}$$

In contrast to FCS, its imaging analogue ICS relies on the fluctuation of the intensity across an image, i.e. it is defined by the difference between pixel intensities at any point in space to the average intensity of an image. As in FCS, ICS functions are calculated for all possible pixel shifts (ξ, ψ) to provide a full spatial correlation function. However, it should be noted that in FCS, one calculates typically over many thousands if not millions of time points, while in ICS, the size of the sample ultimately limits its statistics.

The correlation in fluctuations arises from the non-random structures that are found in the image. As in microscopy, the smallest size of a structure in an image is given by the system's point spread function (PSF), whose radius is given by ω_0. It means that even a point source gives rise to spatial correlations of the size of the PSF. Therefore, pixels should be smaller than the PSF so that the correlations between pixels can be measured. In ICS the correlation function is, thus, fitted with a 2D Gaussian as an approximation for the PSF.

$$G_{ab}(\xi, \psi, 0) = G_{ab}(0, 0, 0)\ \exp\left\{-\frac{\xi^2 + \psi^2}{\omega_0^2}\right\} + G_{ab\infty} \tag{4}$$

Here $G_{ab}(0, 0, 0)$ is the amplitude of the spatial correlation function (SCF), which is inversely proportional to the number of particles in the observation area. $G_{ab\infty}$ is the convergence value for long distances. This is kept as a fit parameter to take account of possible incomplete decay of the SCF. The width of the SCF will be larger than the PSF if particles move during the acquisition of a single frame, something that is better treated in temporal measurements as discussed in later sections, and if there are non-random structures in the image of a size comparable or larger than the PSF.

ICS measures several important parameters. First, ICS determines the size of the PSF if one uses immobile particles that are much smaller than the size of the PSF itself [3]. Second, one can measure the number of particles in the observation area over the amplitude $G_{ab}(0, 0, 0)$. With the knowledge of the size of the observation area and the size of the image, one can count the number of particles [3, 36]. Note that the laser focus needs to be of comparable to the size of the fluorescent entity to capture the cluster density accurately [37].

In principle, several ICS measurements can be taken, and the temporal evolution of the system can be determined. However, the dynamic information is limited because long exposure times are used, or several images averaged to increase the signal-to-noise ratio. It has been shown that for reliable characterization, the temporal resolution must be at least 10 times shorter than the dynamics of interest. Therefore, the reverse is true; any diffusive processes with a time scale longer than the time resolution appear to be static and can be quantified by spatial ICS. In other words, immobile populations contribute to the SCF while fast diffusing populations add to the noise of the SCF. Like confocal FCS, ICS has a concentration limit above

and below data fitting becomes difficult because of a decreasing signal-to-noise ratio. As a rule of thumb, densities of up to 100 particles per μm^2 in a 2D system can be quantified, and this holds for other related techniques [38, 39]. Further, spatial ICS is not a parametric free technique. The experimenter is required to adjust frame-time and the total number of images to compensate for photobleaching and signal-to-noise ratio. The counting capability of ICS combined with gradual photobleaching of fluorophores leads to the so-called pbICS [40] for determining the aggregate distribution of immobilized cluster as demonstrated in CHO cell transfected with green fluorescent protein (GFP)-tagged epidermal growth factor (EGF) receptor. In case of non-optimal acquisition settings, the experimenter can optimize for frame-time and signal-to-noise ratio during the data treatment stage.

A two-colour variant of spatial ICS, spatial image cross-correlation spectroscopy (spatial ICCS), has been introduced to measure colocalization of two different labelled species [41]. Two-colour variation has been employed to study the extent of interactions between two slow-moving species where different macromolecules labelled with two fluorophores of distinct emission wavelength are imaged simultaneously or alternatingly. In fact, ICS is employed behind the scenes in many algorithms. In camera-based microscopy (TIRFM and LSM), the principle of two-colour spatial ICCS doubles up as an alignment tool for the simultaneous two-colour experiment [42]. As it is a purely static method, it limits biology application to immobile and flat samples. An offline analysis tool is available with the JaCoP ImageJ Plugin [43]. Cerutti et al. have shown that ICS can be used to provide quality metrics from a single super-resolution image for evaluation. This method, called QuICS [44], quantitates image quality and can give useful hints on optimizing the imaging conditions.

Recently, the combination of super-resolution and ICCS has been explored. Oneto et al. combined ICCS with STED (STED-ICCS) [45] to estimate the nanoscale distance of nuclear sites with a spatial resolution down to ~50 nm by leveraging the shape of the cross-correlation function shift from the origin. This has been extended to Structured Illumination Microscopy and Image Cross-Correlation Spectroscopy (SIM-ICCS) [46]. Compared to single-molecule localization, the application of super-resolution and ICCS does not provide a complete statistical analysis of distances. Instead, the super-resolution implementation is helpful to analyse average distances between correlated particles in the region.

Up to now, we have discussed ICS mainly as it is performed in a confocal microscope. Nevertheless, it can also be performed in TIRFM with a camera as a detector and improved temporal resolution.

2.2 *Temporal Image Correlation Spectroscopy: TICS*

The temporal variant of image correlation spectroscopy (TICS) takes the same fluorescence microscopy image series as an input (Fig. 1d). Of all variations, it has the closest working principle to FCS. Unlike spatial ICS, TICS does not average

several images. Instead, intensity fluctuations are recorded from frame to frame, correlated in time, and averaged over multiple pixels. This increases time resolution while keeping the signal-to-noise level high. The decay of the temporal correlation function (TCF) reflects the average time that particles require to move in and out of the observation volumes sampled across selected portions of an image; hence, the underlying molecular transport parameters (diffusion coefficient and flow speed) can be extracted [4, 47].

TICS captures the heterogeneity of molecular transport parameters and numbers across raster-scanned regions instead of single points in confocal FCS. However, the ability to sample temporal fluctuations in a larger space comes at the cost of reduced temporal resolution because of the limited confocal scanning speed, therefore imposing an upper limit on diffusion coefficients accessible to TICS. In other words, the fluorophore needs to be within the same beam focal area when the raster scan returns to the same position following the typical ~1 Hz frame rate.

The general correlation function for TICS is given by

$$G_{ab}(0,0,\tau) = \frac{\left\langle \langle \delta I_a(x,\ y,\ t)\delta I_b(x,\ y,\ t+\tau)\rangle_{xy} \right\rangle_t}{\langle I_a\rangle_t \langle I_b\rangle_{t+\tau}} \tag{5}$$

TICS can also be performed as cross-correlation analysis [48, 49] if one records images in different wavelength channels a and b. For autocorrelation analysis in TICS we obtain the following function for diffusion [50].

$$G_{ab}^{\text{diff}}(0,0,\tau) = G_{ab}(0,0,0)\left(1+\frac{4D\tau}{\omega_0^2}\right)^{-1} + G_{ab\infty} \tag{6}$$

where the parameters have the same definitions as discussed in the previous sections. For flow we obtain

$$G_{ab}^{\text{flow}}(0,0,\tau) = G_{ab}(0,0,0)\ \exp\left\{-\frac{(v\tau)^2}{\omega_0^2}\right\} + G_{ab\infty} \tag{7}$$

where v represents the flow speed. For the case that a species of particles undergoes simultaneously flow and diffusion, we obtain a combination of the two previous equations.

$$G_{ab}^{\text{diff,flow}}(0,0,\tau) = G_{ab}(0,0,0)\left(1+\frac{4D\tau}{\omega_0^2}\right)^{-1} exp\left\{-\frac{(v\tau)^2}{4D\tau+\omega_0^2}\right\} + G_{ab\infty} \tag{8}$$

The inclusion of temporal analysis in a stack of frames extends the information available from ICS and allows the measurements of diffusion at least of slow clusters [51]. Using two-photon temporal ICS, diffusion coefficient of as large as 1 μm/s in cell can be measured along with flow [47]. Interesting applications of TICS include

the measurement of nanocarrier motion in live cells [49] or the determination of the mechanosensitive responses of integrin under different conditions over whole cells [52]. Moreover, as two-colour cross-correlation (TICCS) it characterized the recruitment of the proteins deleted in colorectal cancer (DCC) and UNC5B to the plasma membrane after netrin-1 activation [48]. The increased information content provided by TICS came at the cost of temporal and spatial resolution as the time resolution was limited by available acquisition times, and correlation functions were averaged over a user-defined region to improve the signal-to-noise ratio.

2.3 *Spatiotemporal Image Correlation Spectroscopy: STICS*

ICS captures effectively static information from the SCF of an image (Fig. 1b). In contrast, similar to FCS, TICS analyses the fluctuations of particles diffusing through an observation volume (Fig. 1d). As observation volumes are typically rotationally symmetric, no information on the direction of the movement of the particles is captured [53]. Measuring flow directions is possible by cross-correlating pixels intensity in space [51], and thus one needs to capture both spatial and temporal information. In addition, the characterization of flow in a sample requires the determination of multiple parameters. Flow in the sample might not be homogeneous, and a spatially resolved flow profile needs to be measured, comprising information about magnitude and direction, ideally at each point in the acquired image. Spatiotemporal ICS, or STICS, is the first 2D FCS method that captures both spatial and temporal correlations in a temporal series of images as indicated in Eq. 1 and thus can provide complete information of flow profiles [5, 54].

In principle, the spatiotemporal correlation function (STCF) is a function of three (two spatial and one temporal) if not four (three spatial and one temporal) variables. However, as this is difficult to picture, we restrict ourselves to two spatial and one temporal variable and describe the development of the two-dimensional spatial STCF as a function of the temporal variable. In the following discussion of the STCF, we will differentiate several cases. The first will be a static sample without any movement (Fig. 1e). The second will be a sample where particles undergo only diffusion (Fig. 1f(left)). The third sample will have particles under active transport (Fig. 1f (2nd from left)). Here we will assume that these particles are exclusively transported but do not diffuse. Lastly, we will look at particles undergoing flow, assuming that these particles are transported and diffuse (Fig. 1f (3rd from left)). The general equation for STICS is given by

$$G_{ab}(\xi, \psi, \tau) = G_{ab}(0, 0, 0)\left(1 + \frac{4D\tau}{\omega_0^2}\right)^{-1} \exp\left\{\frac{(\xi - v_x\tau)^2 + (\psi - v_y\tau)^2}{4D\tau + \omega_0^2}\right\} + G_{ab\infty} \tag{9}$$

which is the extension of the equation of TICS (Eq. 8) to include the spatial lags ξ and ψ for the x- and y-directions.

In the case of a static sample, STICS reduces to ICS with a time-invariant STCF that peaks at the origin of the spatial variables with the width of the PSF if the particles are much smaller than the PSF. If particles or structures imaged are on the same scale or larger than the PSF, width widens. In the presence of a diffusing particle population, the amplitude of the STCF will remain centred at the origin but with a wider peak representing the movement of the particles during the lag time. In this case, the STCF will increase in width with the increase in lag time, and the rate of the increase in width depends on the mean square displacement of the diffusing particles. In the case of actively transported particles, the STCF will not change shape but move with longer lag times further away from the origin as determined by the transport velocity. If flow is present, the STCF will displace from the origin with time as determined by the flow velocity, but it will also extend in width due to diffusion. Lastly, if multiple populations exhibit different dynamics, then multiple peaks will develop, with each peak representing the characteristics of the movement of one of the populations (Fig. 1f (right)). In practice, the resolution of these multiple populations is not always easy and removing the immobile fraction by Fourier or moving average filtering in the time domain is often necessary to reveal the dynamic population [50].

STICS has been used to analyse flow in microfluidic channels [55], transport of proteins in cells [56–58], kinetics of protein networks [59], and fast and confined diffusion in bacteria [60]. It has also been implemented with two-photon microscopy [61] to measure protein flow in developing *C. elegans* embryos. Furthermore, Pandzic et al. showed that STICS can be used with photo-activation to measure the diffusion of various membrane proteins and that it provides very similar data compared to single-particle tracking (SPT) in photo-activation localization microscopy [62].

As with other correlation methods, STICS can be conducted in a cross-correlation modality between different wavelength channels, leading to spatiotemporal image cross-correlation spectroscopy (STICCS) [63]. STICCS can determine protein interactions, and potentially even transient interactions [63].

In addition to STICS, spatiotemporal dynamics has also been addressed in some related techniques. ICS has been combined with single-particle tracking (SPT) in the so-called particle ICS (PICS), which circumvents the limitations of both SPT and ICS [64]. It can measure at high particle densities, unlike SPT, but has a high spatial resolution, unlike ICS. In another combination of SPT and correlation analysis, the so-called Tracking Image Correlation or TrIC, Dupont et al. analysed 3D tracking data with correlation analysis providing a tool for dynamic colocalization analysis in 3D [65]. Ashdown et al. demonstrated TIRF-SIM imaging can be combined with STICS to quantify molecular flow on subresolution length scales [66]. The high spatiotemporal resolution of these techniques makes them excellent members of the 2D and even 3D FCS toolset.

2.4 k-Space Image Correlation Spectroscopy: kICS

The image in a fluorescence microscope is the convolution of the microscope PSF and the actual distribution of the fluorescent-tagged molecules in the sample. We saw this in the fact that the PSF always limits the STCF in STICS. A common approach to disentangle deconvolutions is transforming the data into Fourier space where the convolution operation is simplified to a product making data treatment much simpler. It is used in k-space ICS (kICS), ICS in the spatial frequency domain, to separate various contributions to the correlation function. By performing the correlation in k-space, Kolin et al. have shown that they can determine the PSF and the diffusion coefficient independently [67].

The second problem in 2D FCS techniques is photobleaching as a whole cross-section of a sample is illuminated with elevated laser intensities – compared to simple imaging – to reach a sufficient signal-to-noise ratio when reading out data at high frame rates. Photobleaching causes a steady decrease in average fluorescence intensity with time. Bleaching can have multiple effects. If bleaching of a molecule is much slower than the time a particle requires to traverse a pixel observation volume, then there is only a general decrease in the overall intensity, which will lead to artefacts in the correlation functions with a time scale determined by the bleaching time. However, if bleaching is so high that fluorescent molecules have a non-negligible probability of being bleached during the transition of a pixel observation area, then the average transit time of molecules will be underestimated, and the diffusion coefficient will be overestimated. The latter form of bleaching is sometimes called cryptic photobleaching.

Over the years, there have been various ways to correct for photobleaching as none of the methods allows analysing uncorrected datasets without imposing bias and artefacts. One way to combat the observational bleaching effects is detrending by normalizing to the first recorded intensity value. Kolin et al. recover accurate diffusion parameters via TICS if the bleaching process is well-characterized as a function of time by a fit function [67]. It is important to note that detrending intensity trace is not the solution to correct cryptic bleaching. In principle, an optimum laser power exists which varies as a function of the diffusion coefficient and observation area. A quick and easy laser power calibration protocol would be a step towards automated fluorescence microscopy [68].

In the presence of photobleaching, kICS has a significant advantage. Under the spatiotemporal image correlation domain, STICS and kICS are similar in their working principle, with some key differences. In k-space, image correlation does not directly correlate fluctuations of image pixel intensities, and instead, it calculates the time-correlation function from a spatially Fourier transformed image. By doing so, kICS overcomes STICS limitations due to photobleaching and photophysics and can separate photophysics and photobleaching from dynamics [69]. Although initially developed for CLSM, kICS can also be applied to TIRFM. Furthermore, kICS can also work with scattering signals, as was shown in the characterization of the intracellular dynamics of gold nanoparticles [70].

Brandao et al. have shown that, in principle, kICS can extract ligand–receptor binding kinetics when certain conditions are met [71]. First, the photophysics, including bleaching and blinking, should be independent of binding and be measurable before the actual experiment. This is fulfilled for many fluorophores but needs to be verified. Second, only receptor-bound ligand should be visible. This second condition can be fulfilled when, for instance, measuring ligand binding to membrane receptors on a TIRFM with relatively slow acquisition rates. The diffusion coefficient for ligands in solution compared to the diffusion coefficient of membrane receptors differs by a factor of about 100. Thus, the fast-moving ligands will contribute a uniform background signal compared to the much slower-moving receptors. Under these conditions, when the photophysics is known, the primary source of unknown fluctuations are the binding and unbinding events of the ligand to the receptor, which can be determined with kICS. Receptor–to-receptor binding and interaction of membrane proteins with membrane domains can also be determined this way [72–74]. This, together with the fact that kICS can measure at a wide range of fluorophore densities, in contrast to other techniques like SPT, that can work only at low concentrations, makes kICS a very versatile technique to measure membrane events.

Originally, ICS variants were conducted at limited spatial and temporal resolution. Acquisition times at video rates allow only measurement of slow diffusing particles, e.g. membrane proteins. But they were also performed at limited spatial resolution as a minimum dimension is necessary to calculate spatial correlations. Nevertheless, this is not a fundamental limit as modern cameras allow fast read-out with time resolutions less than 100 μs per region of interest, containing hundreds to thousands of pixels. The pixels and frames can then be binned to optimize the data for different evaluation techniques, including 2D FCS modalities. With the new technology and advances in computation, these techniques will be able to also measure cytosolic or extracellular protein diffusion in cells and organisms and can be extended to 3D.

2.5 Image Mean Squared Displacement: iMSD

Biological systems are generally inhomogeneous, leading to anisotropy in transport and diffusion, as particles encounter different environments in different directions or are hindered by obstacles. In that case, directional analysis of particle mobility is required. This can be provided in scanning and imaging approaches, in which, e.g., flow profiles were measured, as discussed in the next section. But this can also be addressed in image-based approaches by analysing the spatial cross-correlations between different points in an image. For this purpose, a technique called image Mean Squared Displacement (iMSD) was introduced [75–77].

iMSD is a STICS modality in which the spatial correlations in all directions are analysed in time with respect to a particular point. This can be achieved in scanning systems as well as in multi-pixel detection systems. The calculations are performed

on a polar grid, and values are calculated over a limited number of angles. This allows averaging more pixels the larger the distance from the central pixel, improving the signal-to-noise ratio. This kind of analysis allows to determine a direction-dependent measurement of transport and diffusion and provides a connectivity map of a sample, identifying obstacles to diffusion and transport [78].

In another application, iMSD was used to evaluate the spatial analogue of the FCS diffusion laws [79, 80] to analyse the diffusive modes of molecules in the cytoplasm [76]. If diffusion is length scale-dependent, e.g., when obstacles and trapping sites are present, then an analysis of the diffusion coefficient with length scale can identify diffusion mode. In analogy, different diffusive modes measured over the same length scale but at different time scales will show a similar dependency, which can be used in iMSD at different scan speeds to identify diffusive modes. In work combining most of the ICS techniques, including iMSD and RICS (see next section) discussed here, Hendrix et al. analysed the HIV-1 Gag polyprotein assembly in live cells using a customized confocal system [81]. This work shows the differences in applications of the various ICS techniques but also demonstrates that many of them can be applied to the same data.

Finally, iMSD was recently also implemented on a confocal microscope with an Airyscan [21], or multi-element single-photon avalanche diode [22] detector, allowing much faster acquisitions and widening the possibilities to measure dynamics with iMSD.

2.6 Pair Correlation Function: pCF

Pair correlation function (pCF) analysis is a special case of spatiotemporal correlations, in which two points in space are correlated in time. If the two points are sufficiently far apart so that their observation volumes do not overlap, the resulting pCF will possess a peak at the time it takes fluorescent probes to move from one location to the other [82]. In principle, this approach can be applied to any data that has some inherent spatial and temporal information, including line scanning, multifocus, and imaging approaches. The probability that a particle that originated at (x_0, y_0, z_0) at time t is found at location (x_1, y_1, z_1) at a time $t + \tau$ is given by the diffusion propagator

$$P(r, \tau) = \frac{1}{(4\pi D\tau)^{3/2}} \exp\left\{ - \frac{(x_1 - x_0)^2 + (y_1 - y_0)^2 + (z_1 - z_0)^2}{4D\tau} \right\} \qquad (10)$$

At a particular distance $r = \sqrt{(x_1 - x_0)^2 + (y_1 - y_0)^2 + (z_1 - z_0)^2}$ between two points (x_0, y_0, z_0) and (x_1, y_1, z_1), this function will peak for a time τ that depends on the diffusion coefficient D and which can be calculated from the mean squared displacement, $\langle r^2 \rangle = 6Dt$. The corresponding pair correlation is

$$G(\tau) = \frac{\langle \delta I(x_0,\ y_0,\ z_0,\ t)\delta I(x_1,\ y_1,\ z_1,\ t+\tau)\rangle_t}{\langle I(x_0,\ y_0,\ z_0,\ t)\rangle_t \langle I(x_1,\ y_1,\ z_1,\ t)\rangle_{t+\tau}} \tag{11}$$

where the strength of the correlation depends on how many particles have diffused from the first to the second point at time τ as described by the diffusion propagator.

If there are obstacles between the two locations, the peak will occur later depending on how long a probe will need to bypass the obstacle. In the extreme case that a barrier exists that prevents probes from translocating from one point to the other, the pCF will be zero. This principle was used to measure molecular transport across nuclear pore complexes [83], and in the cellular nucleus at different chromatin densities, during different cell cycle stages, and during DNA repair [84–86]. This work nicely demonstrated the advantage of spatiotemporal correlations as single-point FCS only measures local mobility but not long-distance transport. The use of pCF allows the determination of intracellular as well as membrane organization [87, 88] and was used in plants to measure the movement of transcription factors [89]. The method was extended to 2D to measure anisotropic movement [78]. It should be noted that instead of calculating the temporal pCF for two positions, one can also calculate the spatial pCF at a particular time, describing the variation of molecular densities in space [90].

3 Scanning FCS

FCS was originally conceived as a single-point measurement, but it was early on realized how sample flow or laser scanning can provide extra information [6]. In the most simple case, flow or scanning increases sample throughput [91, 92]. But of interest in this chapter is the inclusion of spatial information into the originally temporal FCS measurements. We will therefore progress from simple scanning FCS approaches that provide 1D spatiotemporal information, to more complex scanning patterns that provide 2D spatiotemporal information, to finally RICS (Fig. 1c) that uses the inherent time structure in confocal images to obtain the same information but from readily commercially available instrumentation [15]. RICS thus made spatiotemporal correlations widely available. The different approaches have their own advantages and disadvantages and show different ways of monitoring fluctuations depending on the data collection method.

3.1 Scanning FCS in the Presence of Immobile Particles

FCS is insensitive to immobile or very slowly moving particles as these do not cause fluctuations and thus cannot be detected in the correlation functions. However, a fluctuating signal even from immobile particles can be obtained when one either

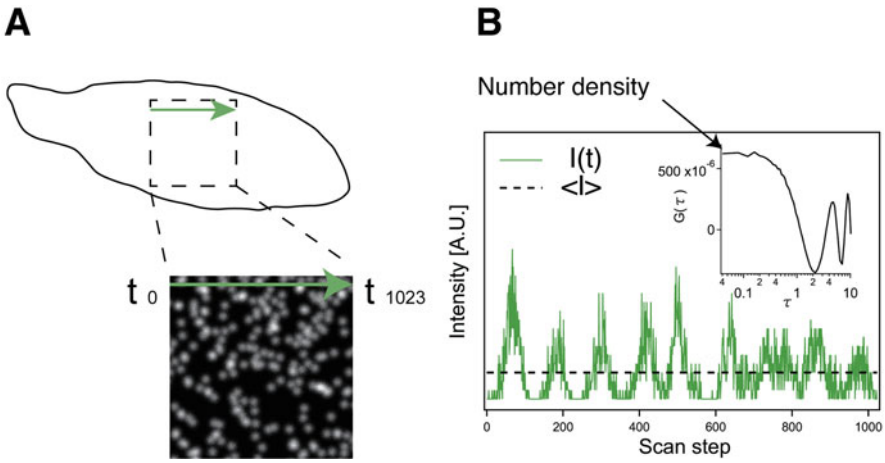

Fig. 2 Principles of scanning FCS for immobile particles. (**a**) An illumination spot with calibrated beam radius (w_0) is scanned across a sample either by confocal or stage scanning at a known speed. (**b**) The start of the line scan t_0 is synchronized with the data acquisition. The TCF decay shows the characteristic scan speed, while the amplitude is related to the particle density

moves the sample, e.g. by stage scanning or by driving some movement in the sample, or by scanning the beam. Weissman et al. developed a similar concept to measure molecular weights of macromolecule [93] although it differed in experimental configuration.

In 1986, the first implementation of Scanning Fluorescence Correlation Spectroscopy (SFCS) arose by translating samples linearly and horizontally by a translation stage while fixing the illumination beam (Fig. 2a). Petersen et al. successfully employed this configuration to extract aggregation/cluster size and the density of clusters from a line segment of a cell [7], aggregation of virus glycoproteins [8], ligand binding [9], and EGFR distribution on the cell plasma membranes with an average of 130 receptors per cluster and 7–8 clusters per μm^2 [10].

FCS statistical accuracy [94] depends on the signal-to-noise ratio and thus on the number of photons detected per detection interval and the square root of data points.

For SFCS, one can scan slowly and thus increase the counts per second. However, the scan range is limited by the physical dimension of the sample (~20 μm in the case of mammalian cells), while the characteristic fluctuation width is defined by the dimension of the focused laser beam, yielding at best some tens of fluctuations per scan. Therefore, multiple independent scans need to be averaged to improve the accuracy of immobile particle analysis.

To understand how this is done, let us take a look at the relevant correlation functions. The basic correlation function for confocal microscopes describing diffusion in 2D is

$$G_{2D\ \mathrm{diffusion}}(\tau) = \frac{1}{N}\left(1 + \frac{4D\tau}{\omega_0^2}\right)^{-1} + G_\infty \tag{12}$$

where D is the diffusion coefficient and w_0 is the e^{-2} radius of the laser focus. In the case of sample flow or when the laser focus is scanned at a constant speed in the focal plane, and the absence of diffusion the equation changes to [6].

$$G_{2D\ \mathrm{flow}}(\tau) = \frac{1}{N}\ \exp\left\{-\frac{\left(v_x^2 + v_y^2\right)\tau^2}{\omega_0^2}\right\} + G_\infty \tag{13}$$

where v_x and v_x describe the flow/scan speed in the x and y direction. The only unknown in this equation is the number of particles N, which measures the number of particles per observation volume observed on average and which can be obtained by fitting the experimental curve (Fig. 2b). If one has an estimate of the total number of monomers in the sample, then the aggregate size can be determined. However, one has to assume that the fluorescence is not altered in the aggregates compared to the monomeric state, that all molecules are fluorescent, and that photobleaching is negligible, as otherwise, the estimates will be biased to lower numbers.

Scanning FCS for the characterization of immobile particles provided estimates of the mean number of virus glycoprotein aggregates from Sindbis virus and vesicular stomatitis virus [8] and was later extended to measure cell surface receptor aggregation [9, 10]. The method was applied to 2D CLSM images [39] and extended to other microscopy technique which does not necessarily require scanning. For instance, Number and Brightness analysis [95] revealed the presence of a large bright immobile aggregate within a heterogeneous region of a sample.

3.2 Scanning FCS in the Presence of Flow

If flow is present in a sample in which the particles themselves also diffuse, then we obtain a correlation function which is a combination of the ones derived for flow and for diffusion:

$$G_{2D\ \mathrm{diff,\ flow}}(\tau) = \frac{1}{N}\left(1 + \frac{4D\tau}{\omega_0^2}\right)^{-1} \exp\left\{-\frac{v^2\tau^2}{4D\tau + \omega_0^2}\right\} + G_\infty \tag{14}$$

However, as the confocal volume is rotationally symmetric, Eq. 14 does not allow us to determine the flow velocity $\vec{v}_{\mathrm{flow}}$ and direction of flow (θ), as the correlation function is independent of the flow direction. The flow direction and thus the velocity can nevertheless be determined if one measures the correlation function with a stationary beam to determine the flow speed (Fig. 3a) and then in a second

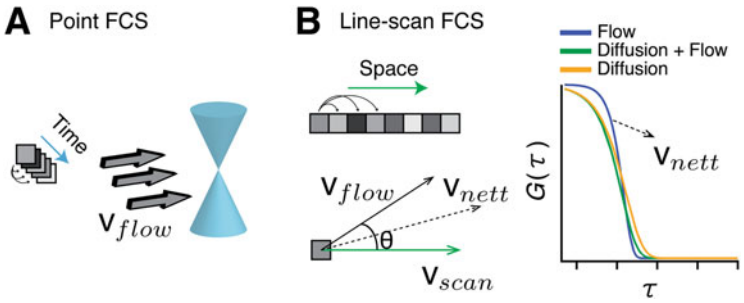

Fig. 3 Flow measurement. (**a**) Using a stationary beam, the flow speed can be determined as particles are driven through the focus and thus influence the shape and width of the autocorrelation function. (**b**) Scanning the beam in the sample leads to a characteristic change in the ACF as the flow ($\boldsymbol{v}_{\text{flow}}$) and scan ($\boldsymbol{v}_{\text{scan}}$) add up to a new effective speed ($\boldsymbol{v}_{\text{nett}}$) from which the angle between scan and flow can be determined

measurement (Fig. 3b) determines the correlation function in the presence of a known scan speed [11]. In that case, the correlation function changes to

$$G_{2D\ \text{diff,flow,scan}}(\tau) = \frac{1}{N}\left(1+\frac{4D\tau}{\omega_0^2}\right)^{-1} \exp\left\{-\frac{\left(\vec{v}_{\text{flow}}+\vec{v}_{\text{scan}}\right)^2\tau^2}{4D\tau+\omega_0^2}\right\} + G_\infty \tag{15}$$

and one can determine the velocity according to the following equation:

$$\vec{v}_{\text{nett}}^{\,2} = \left(\vec{v}_{\text{flow}}+\vec{v}_{\text{scan}}\right)^2 = \vec{v}_{\text{flow}}^{\,2} + \vec{v}_{\text{scan}}^{\,2} + 2\,\vec{v}_{\text{flow}}\,\vec{v}_{\text{scan}}\cos\theta \tag{16}$$

The sequential strategy to determine flow and its directionality can be extended to 3D with three measurements, a stationary measurement to determine the flow speed and one in plane and on axial scan [12].

As a rule of thumb, the separation of diffusion and flow (Fig. 3c) is possible if the average time it takes a particle to traverse the focal volume by diffusion and by flow is within a factor 10 of each other. Otherwise, the faster process dominates to the extent that the slower one cannot be determined anymore. Line-scan FCS was used to characterize flow profiles in microfluidic channels and blood flow direction in living zebrafish with an accuracy down ±10° [11].

Cross-correlation has proven to be a valuable tool to elucidate vectorial flow information and, in the case of diffusion, yields absolute values without knowledge of the PSF of the system. The technique has been applied to a flow system with two spatially separated volumes using scattering of two wavelengths [96] or fluorescence with a single wavelength [17]. Since the maximum cross-correlation is proportional

to the average time a molecule takes to move from a specific location to another, one can tune the time resolution of the technique by changing the distance between the two foci. As in line-scan FCS, directional information can be extracted by changing the direction of the placement of the point in the sample.

As line-scan FCS determines flow characteristics only in one direction, circular-scan FCS was developed. In circular-scan FCS, one can cross-correlate opposite points on the scan path to obtain directional information. Circular-scan FCS thus produces a map of molecular flows indicating if barriers are present [97, 98]. Since the laser beam is scanned repeatedly over the different locations, information is limited to the scan orbit with a resolution given by the size of the laser focus. The equation for circular-scan FCS is given by

$$G_{2D\ \mathrm{diff,circular\ scan}}(\tau) = \frac{1}{N}\left(1 + \frac{4D\tau}{\omega_0^2}\right)^{-1} exp\left\{-\frac{4\rho^2 \sin\left(\frac{\omega t}{2}\right)^2 \tau^2}{4D\tau + \omega_0^2}\right\} + G_\infty \quad (17)$$

In circular-scan FCS, the experimenter can choose radius (ρ) and angular scan frequency (ω) of the scan and produce intensity traces for each position on the scan and has the option to evaluate the data as auto- or cross-correlations as required. There are at least two ways to perform data analysis to study sample dynamics quantitatively.

Ruan et al., for instance, leveraged temporal and spatial information along the circular path independently [99]. With this approach, the confocal volume is scanned circularly at speed much faster than the particle needs to diffuse through a single location, resulting in a set of correlation functions from all points along the scanned path. This method recovers diffusion coefficients in giant unilamellar vesicle (GUV) membranes up to 20 $\mu m^2/s$ with the same precision as conventional FCS measurement. On the other hand, Petrasek et al. used the inherent spatiotemporal information in circular scanning to address the need for calibration of the focal volume and the problem of focusing on membranes. They suggested spatially cross-correlating points on the circular-scan path with a known diameter 2 ρ and a size smaller than 1 μm. This was successfully applied to determine diffusion coefficients ranging from dyes in solution [100] to slower diffusion in model membranes [101]. This approach to measuring diffusion is independent of the size of the focal volume and is not sensitive to the position of the membrane with respect to the focal plane but comes at the cost of more limited spatial information (Eq. 17).

While both scanning paths can be applied, circular scanning has some essential advantages. First, the statistics are no longer limited to the scanned path. Second, a broader range of dynamics can be observed [101] compared to earlier work [11]. Third, the autocorrelation can be easily computed with the existing algorithm without synchronizing data acquisition with the line scan.

3.3 *Scanning FCS as a Tool for Multiplexing and Avoidance of Artefacts*

Scanning FCS with line or circular patterns (Fig. 4a) can also provide FCS measurements at multiple points, i.e. along the scan path. The spatial realization first came by continuously scanning the laser beam across a sample in a line (Fig. 4c) or circle (Fig. 4d) while the emitted light from each spatial location was recorded in sequence, providing an intensity carpet. The intensity time-trace at each spatial location is then correlated in time with the temporal resolution given by the scanning frequency. At each location, one thus obtains information about diffusion.

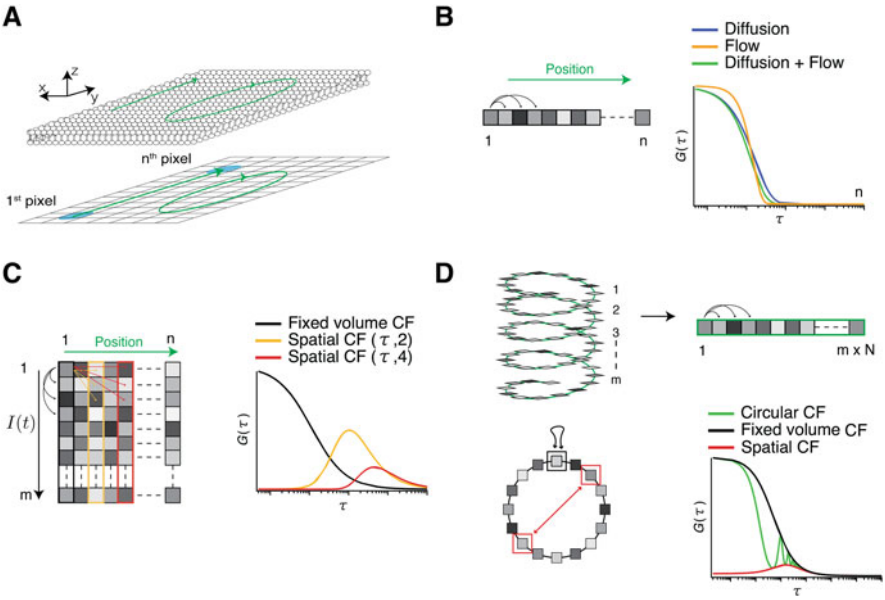

Fig. 4 (**a**) Laser scanning can be performed in various patterns, here shown as linear or circular scan. (**b**) A linear scan can be analysed continuously in time without explicitly using spatial information. In this case, a single autocorrelation function is calculated for all scan repeats. While this is experimentally simple, it provides only information on diffusion and flow speed. (**c**) Spatial information can be used by arranging multiple scans in an intensity carpet ordered according to the position in the sample along with the scan and different times they were recorded in the repeat scans. Auto- and spatial cross-correlation functions provide information about diffusion, flow, and connectivity in the sample. (**d**) In circular scanning, the same information can be obtained. Calculating the time autocorrelation function shows characteristic repeating peaks when the laser beam returns to the same point (*green line*). Two extremes envelop this function, first the autocorrelation function for a beam with the radius of the scan circle (*black line*), and second the spatial cross-correlation function between two points on opposite ends of the circle (*red line*). The two enveloping correlation functions are obtained by setting the *sin* function in Eq. 17 to either 0 or 1

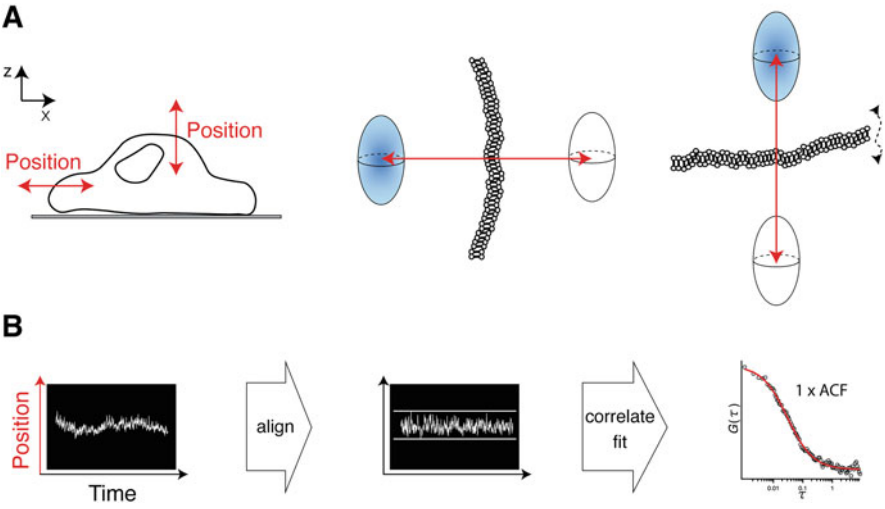

Fig. 5 Line scanning to reduce artefacts of sample movement. (**a**) The observation volume can be scanned laterally or axially across a fluctuating membrane. (**b**) Once per scan, the observation volume is on the membrane. These points are selected, aligned in time and then correlated to provide a correlation function. The time resolution, in this case, is limited to the time for one scan. However, the correlation function does not suffer from sample movement artefacts as only points on the membrane are correlated

This approach allows FCS multiplexing, but at the expense of temporal resolution since the observation volume returns to the same spot only once per scan. When 10–100 points are scanned, diffusion coefficients of about 0.05–1 $\mu m^2/s$ can be determined, enough to cover lipid membrane measurements and slow-moving complexes in solution. Software to process local ACFs from confocal scanning data is available as FoCuS-scan [102]. An alternative approach is represented by scanning the beam slowly across the sample. In this case, one can calculate the correlations within short time segments. The segmented FCS data can be combined to extract average diffusion values in specific compartments.

Di Bona et al. have used this approach to detect the small variations of diffusion of GFP in heterochromatin vs euchromatin [103]. Overall, SFCS is particularly useful for slower dynamics and is insensitive to photobleaching as the illumination beam spends very little time per observation volume.

Besides reducing sensitivity to photobleaching, scanning FCS can also be employed to remove movement artefacts. If the sample to be measured moves within a limited range, then scanning the laser beam over this range can ensure that the sample is captured at least once per scan (Fig. 5a). Cellular plasma membranes, for instance, have a tendency to undulate or move perpendicular to the membrane surface. In a point measurement, this will lead to large fluctuations in the signal due to the membrane movement, and thus artefacts in the correlation function [104]. By scanning the confocal volume perpendicular to the membrane, one can

locate the position of the membrane in each scan. By aligning the data collected when the beam is on the membrane, their temporal correlation yields information about processes slower than the scan rate. In this modality, line-scan FCS sacrifices the multiplexing aspect to produce a single correlation function that is free from movement artefact (Fig. 4b).

Recent application of scanning a line in the z-direction, i.e. the optical axis of the microscope, has also been used to overcome sample movement and photobleaching artefacts [105] and was used to determine equilibrium dissociation constants (*Kd*) of ligand–receptor interactions in the Wnt signalling pathway at near-native amounts [106].

Scanning with two foci of different wavelengths, either in continuous-wave excitation or with pulsed interleaved excitation, can determine membrane dynamics and binding interactions with the advantage of reduced artefacts as discussed before [104]. This was used in combination with atomic force microscopy (AFM) to study rafts in model membranes [107]. Moreover, in live zebrafish embryos, in vivo binding affinities of Fgf8 to its receptors, Fgfr1 and Fgfr4 were measured [108]. In combination with STED, called axial ls-STED-FCS, time resolution on the μs-scale and spatial resolution of ~50 nm were achieved using tunable acoustic gradient index of refraction lenses [109]. Dual-colour dual-focus line scanning was applied in Wnt signalling pathway study to quantify ligand–receptor concentration, and diffusion coefficient without the need for a separate observation volume calibration [110].

3.4 Raster Image Correlation Spectroscopy: RICS

Scanning FCS utilizes the temporal and spatial information in a scan. In these applications, typically, the scan speed was uniform along a line or circular path. Nevertheless, even a confocal image contains an inherent time structure, with different time constants and the two perpendicular scan directions, that can calculate correlation functions. The fast scan direction is similar to the line-scan FCS with small delays τ_p between the acquisition of neighbouring pixels. However, when moving to the next line, the delay between the pixels of neighbouring lines, τ_l is much longer, depending on the time to scan one line. RICS uses this inherent time structure to calculate spatiotemporal correlation functions over small regions of interest (Fig. 6a).

To see how this works, let us look at the time structure of a confocal image. The time delay between any two pixels depends on their distance on the image grid. If we call the spatial lag, measured in number of pixels, in the fast scan direction ξ and the spatial lag in the slow scan direction (i.e. the lag in number of lines) ψ, then the time delay between these two pixels will be given by $\tau_p.\ \xi + \tau_l.\ \psi$, the RICS correlation function can thus be expressed as a correlation function of the spatial lags, which inherently defines the time dependence.

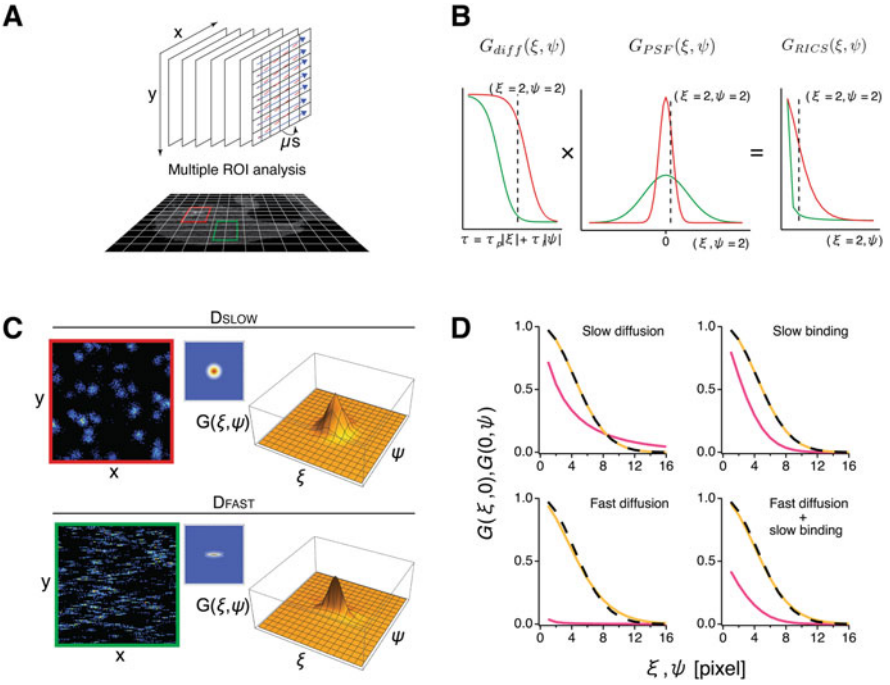

Fig. 6 Schematic illustration of a RICS experiment. (**a**) Rastered scanned image(s) can be analysed over multiple regions of interest (ROI) to create parameter maps. (**b**) The first two graphs show the different RICS correlation function components for diffusion and the PSF. The third graph shows the combination of the two. The red and green lines show the characteristic correlation function over the slow and fast regions. (**c**) RICS simulation and analysis for slow and fast-moving particles performed with simFCS3 [111]. The graph on the right shows the resulting 2D spatiotemporal correlation functions. (**d**) RICS allows binding to be discriminated against diffusion, provided binding/unbinding is much slower than diffusion. RICS cross-sections along and perpendicular to the scanned direction are plotted in orange and pink. The dotted curves stand for the PSF profile

$$G_{RICS}(\xi,\psi) = \frac{\langle \delta I(x,\ y)\delta I(x+\xi,\ y+\psi)\rangle}{\langle I\rangle^2} \tag{18}$$

The RICS correlation function (Fig. 6b (right)) contains now at least two contributions. First is the decay of the correlation function for diffusion (Fig. 6b (left)) due to the time delay between two pixels. Second, the broadening of the PSF (Fig. 6b (middle)) due to particle movement as we have seen before in the section on ICS.

In confocal FCS the correlation function for diffusion in 3D is given by (Magde 1974):

$$G_{FCS}(\tau) = \frac{\langle \delta I(t)\delta I(t+\tau)\rangle}{\langle I\rangle^2} = \frac{1}{N}\left(1+\frac{4D\tau}{\omega_0^2}\right)^{-1}\left(1+\frac{4D\tau}{\omega_z^2}\right)^{-\frac{1}{2}} + G_\infty \tag{19}$$

Here G_∞ is the value of the correlation function at long times, which is ideally 0 but is typically used as fitting parameter as the ideal value is only reached for infinitely long times. In RICS, due to its particular time structure, this component is

$$G_{\text{diff}}(\xi,\psi) = \frac{1}{N}\left(1+\frac{4D\left(\tau_p|\xi|+\tau_l|\psi|\right)}{\omega_0^2}\right)^{-1}\left(1+\frac{4D\left(\tau_p|\xi|+\tau_l|\psi|\right)}{\omega_z^2}\right)^{-\frac{1}{2}} \tag{20}$$

The second component describing the broadening of the PSF due to particle diffusion is given by

$$G_{PSF}(\xi,\psi) = exp\left\{-\frac{a^2\left(\xi^2+\psi^2\right)}{4D\left(\tau_p|\xi|+\tau_l|\psi|\right)+w_0^2}\right\} \tag{21}$$

where we denote the size of a pixel by a, note that if there is no diffusion, this equation will describe the PSF (Eq. 4). Putting this together, we obtain the correlation function for RICS

$$\begin{aligned} &G_{\text{RICS}}(\xi,\psi) \\ &= \frac{1}{N}\left(1+\frac{4D\left(\tau_p|\xi|+\tau_l|\psi|\right)}{\omega_0^2}\right)^{-1}\left(1+\frac{4D\left(\tau_p|\xi|+\tau_l|\psi|\right)}{\omega_z^2}\right)^{-\frac{1}{2}} \\ &\times \exp\left\{-\frac{a^2\left(\xi^2+\psi^2\right)}{4D\left(\tau_p|\xi|+\tau_l|\psi|\right)+w_0^2}\right\}+G_\infty \end{aligned} \tag{22}$$

Other processes, e.g. blinking or binding, can be included in the correlation function as well [112]. This correlation function is very similar to the correlation functions for STICS (Eq. 9) and scanning FCS (Eq. 15). However, in RICS, we have explicitly taken the third axial dimension into account, as RICS can acquire sufficiently fast to measure diffusion in solution (Fig. 6c). An interesting point about RICS is that it covers different temporal ranges as the temporal delays in different image directions are different by 1–2 orders of magnitude. Moreover, these time ranges can be tuned by the scanning speed to acquire the data in a suitable range for the probe under investigation. Note that for RICS the pixel size is set smaller than the PSF, and multiple frames are averaged, especially in the case of small regions of interest. Other measures such as filtering immobile structures to detect better-diffusing particles were performed in the time domain by averaging images and subtracting the average image from each frame [15].

A two-colour variant called cc-RICS has been used to quantitatively evaluate the fraction of intact DNAs with both green and red fluorescence in living cells [81, 113, 114]. Compared to FCS/FCCS, such image-based RICS/cc-RICS has the advantage to allow monitoring of diffusion dynamics, reaction kinetics, and molecular interaction at multiple ROIs [115–117].

As RICS is implemented on a confocal microscope, it can be easily integrated with stimulated emission depletion (STED) microscopy providing simultaneous super-resolution and dynamics measurements [118, 119]. It is by now also possible to scan random areas [115]. For more details on its implementation and evaluation of RICS characteristics, we refer the interested reader to the literature [111, 120].

The fact that RICS can be used with commercially available confocal microscopes without any customization is a major advantage, and it consequently has been widely used. Among others, RICS has been used to detect binding (Fig. 6d) to adhesions and scaffolds [112, 121] and to measure lipid dynamics in cell membranes [122–125].

4 Multipoint and Imaging FCS

The idea to record multiple points for FCS simultaneously is an obvious extension of single-point confocal FCS, although not easily implemented as mentioned earlier. The availability of array detectors with a large number of detection elements and sufficiently fast read-out changed that situation. By using a spinning disk confocal microscope with a resting spinning disk to create multiple confocal areas, this was extended to ~1,000 detection elements [126]. This approach has recently culminated in the so-called massively parallel FCS (Fig. 7a), where a diffractive element creates a grid of confocal points and the signal is detected by recently developed single-photon avalanche diode (SPAD) arrays, where each pixel functions as its own pinhole and detector [127, 128]. This approach has the advantage of having large numbers of detection elements and having excellent time resolution sufficient even to measure fluorescence lifetimes, which other array detectors, especially cameras, cannot reach. Oasa et al. combined FLIM with massively parallel FCS (mpFCS) to characterize the diffusion across a cell of oligodendrocyte transcription factor 2 [129].

However, all these approaches use confocal illumination schemes. As the laser beams in confocal schemes are highly focused and traverse the whole sample as they converge before and diverge after the focal point, they create significant cross-talk for neighbouring pixels (Fig. 7a), a problem long known for spinning disk confocal microscopes [130]. For FCS this sets various lower limits on the minimum spacing between pixels required to avoid cross-talk between neighbouring pixels [29]. If pixels, and thus laser beams, are too close, the signal detected in one pinhole will stem from multiple laser beams, increasing the cross-talk and the effective observation volume, making the measurement of fluctuations necessary for FCS impossible. But even if ACFs can be recorded for each pinhole, the pixels need to be far enough apart to avoid an influence of the sample observed by one pixel to influence the shape of the ACF of the neighbouring pixel. One needs at least two photons from a particle for a correlation. Therefore, as long as a pinhole can detect two photons from a molecule in a neighbouring laser beam, it will lead to extra correlations in the ACF. However, more stringently, to avoid an influence of the cross-talk on the amplitude

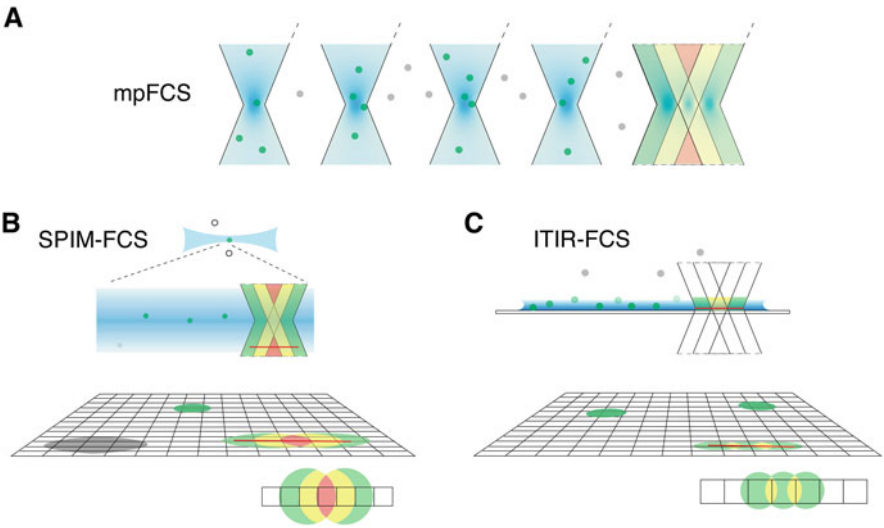

Fig. 7 Illumination scheme of various FCS multiplexing methods. (**a**) Simultaneous excitation and detection of fluorescent molecules in multiple confocal spots (mpFCS). The observation volumes have to be placed at a certain distance to avoid cross-talk. On the right, three observation volumes are placed contiguously in the sample. As indicated by the colours, some parts of the sample are illuminated and detected by all three observation volumes (*red*), some by two (*yellow*), and some by only one *green*. Note that because the laser beam in a confocal setup propagates through the whole sample, and thus the amount of cross-talk depends on the sample thickness, which is typically on the μm scale. (**b**) The use of light-sheet illumination and array detectors in SPIM-FCS. As the illuminating light sheet is only ~1 μm thick, cross-talk is limited, as indicated again by the colour-coded observation volumes, and contiguous pixels can be used. Nevertheless, the cross-talk will change the correlation function and needs to be accounted for. Cross-talk between pixels is indicated at the bottom of the graph. (**c**) In Imaging Total Internal Reflection FCS (ITIR-FCS), optical sectioning is based on the confinement of the evanescent wave generated at the glass/water interface. In ITIR-FCS the cross-talk is limited by both, the sample which is typically a membrane with ~5 nm thickness, or if measuring in solution by the exponentially decaying evanescent wave of ~100 nm thickness. Cross-talk between pixels is indicated at the bottom of the graph

(not the width or shape) of the ACFs, the pixels need to be even further apart. Although single photons are not enough for a correlation, uncorrelated single photons will contribute to the background and thus lower the ACF amplitude. These restrictions limit the number of pixels that can be used in confocal approaches.

A partial solution to the problem was found with new detection schemes that illuminate only a cross-section of limited thickness in a specimen. This can come in the form of TIRF (Fig. 7c (top)) with only ~100 nm above the cover slide illuminated [32, 131], or in light-sheet microscopy (Fig. 7b (top)) with light-sheet thicknesses of ~1 μm [132]. This minimizes cross-talk between pixels as only single sections of the sample are illuminated, and no signal from the bulk or other parts of the sample is excited and detected. This then allows the use of cameras with contiguous pixels as detectors [29, 30]. It should be noted that neighbouring pixels will still be correlated to some extent due to the finite size of the PSF, and the image of one molecule can

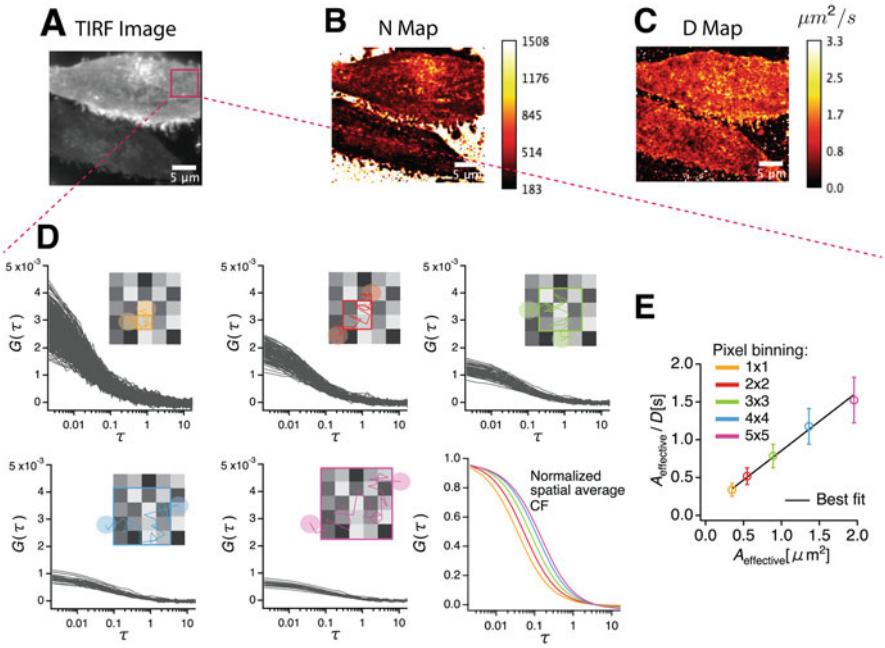

Fig. 8 Study of sample organization by Imaging FCS. (**a**) TIRFM image of PMT-mEGFP showing two CHO-K1 cells at different expression levels (TIRFM image displayed as average intensity z-projection for clarity). Each pixel was temporally correlated and fitted, and quantitative parameters are rendered as heat maps for (**b**) the number of particles *N* and (**c**) the diffusion coefficient *D*. (**d**) Imaging FCS allows pinhole size selection during data treatment by pixel binning. The autocorrelation function amplitude decreases (*left top) to (middle bottom)*. Furthermore, its width increases (*bottom right*) with the increase of the effective observation area. (**e**) Diffusion and its length-scale dependency to identify diffusive modes

always span at least neighbouring pixels (Fig. 7b, c (bottom)), and imaging FCS takes account of these effects in their data evaluation. But this effect is limited and is similar to the effect of the PSF in imaging. However, camera-based FCS, although allowing for the recording of contiguous pixels in a sample and thus creating full spatial maps (Fig. 8b, c), can do so only at a much lower time resolution. Most experiments in Imaging FCS have been performed at ~ms time resolution, although a resolution down to 0.02 ms has been reached [33, 133].

Imaging FCS was calibrated against a range of other techniques to ensure consistency of its results with the main techniques used to measure diffusion and diffusion modes [134–137] and was applied in a variety of contexts [35]. Cooper et al. measured the diffusion at liquid–solid interfaces and determined molecular interaction kinetics with surfaces [138]. Xu et al. measured diffusion within nanotubes and determined the influence of charge on molecular transport [139], Erstling et al. determined the photophysics of nanoparticles [140], and several applications for the characterization of lipid bilayers were reported [134, 141]. In

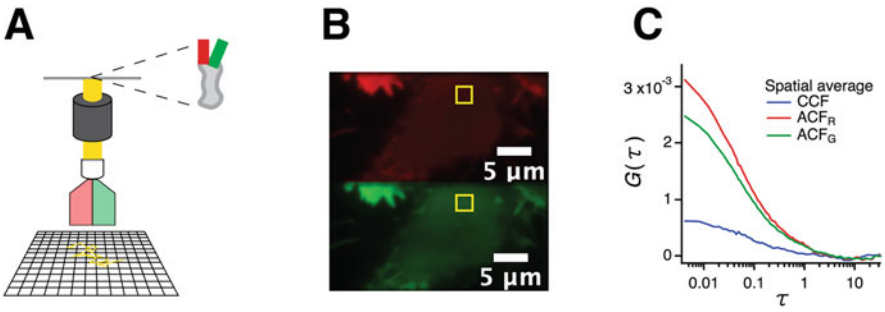

Fig. 9 DC-ITIR-FCCS modality [136]. (**a**) Schematic of TIRFM instrumentation coupled with an image splitter device to capture images of PMT-mEGFP-mApple into wavelength channels at 500 fps. (**b**) Image of double-labelled plasma membrane targeting PMT-mEGFP-mCherry displayed on two halves of the camera chip. (**c**) The double-labelled protein yields a positive cross-correlation in HEK cells; the auto- (*green* and *red*) and cross-correlation (*blue*) functions displayed are the spatial average across a selected ROI (in *yellow*)

the life sciences the interaction of peptides with lipid bilayers [142] and cell membranes [143] and the characterization of membrane receptor diffusion are typical applications of Imaging FCS [144–146]. By pooling several Imaging FCS measurements, Bag et al. obtained very precise diffusion coefficient measurements of lipids and membrane proteins in live cells [147, 148]. Imaging FCS was also used in developing small organisms to determine cytoplasmic and membrane diffusion [133, 149–151], and in biofilms to characterize diffusion in dependence of size and charge of diffusants [152]. In the form of Imaging FCCS (Fig. 9) it measured interactions of proteins in live cells [149, 153, 154].

This brings us to the question of what advantages or extra information these FCS modalities provide. The obvious answer is multiplexing. The approaches described in this section provide thousands of points routinely simultaneously, and even more than one million points in a single measurement have been achieved (Wohland unpublished data). The measurements can also be performed with two colours allowing to perform FCCS with a single array detector with excitation either in a continuous [149, 153–155] or interleaved manner (Wohland unpublished data).

A further advantage is that – similar to what was earlier mentioned in confocal microscopy with multipoint detectors for a single detection element – the data on array detectors can detect different parts of a sample and determine whether there is existing flow or transport [29] or characterize anisotropic diffusion [156]. Furthermore, the pixels on a camera can be binned to provide observation areas and volumes of different sizes [29]. The FCS diffusion law (Fig. 8e) can be used to determine the length-scale dependence of diffusion and thus determine the particular diffusion mode the particle is undergoing [79, 157, 158]. In 2D FCS and especially Imaging FCS this can be easily achieved as only one set of data is needed, and various binning sizes (Fig. 8d) can be applied to the existing data to create different observation areas [134, 141, 145, 159–161]. Thus, FCS diffusion law analysis can

be derived from a single measurement and can be even performed on multiple areas of a cell [145]. Nevertheless, these approaches based on array detectors have wider applicability. By recording the maximal possible amounts of photons with as high spatial and temporal resolution as possible, one is not restricted to perform exclusively FCS but can evaluate the data in each or between any pixels or group of pixels with whatever analytical tools available. So it was already shown that FCS can be combined with super-resolution microscopy [162, 163] and simultaneously with other fluctuation or single-molecule fluorescence techniques [135, 162, 163].

Another approach that provides binding kinetics and that is at the origin of many of the techniques discussed here is the combination of TIRFM with FCS with single-point detection [164–167]. Although not strictly 2D, several studies have demonstrated the application of TIRF-FCS to measure biomolecular diffusion in membranes and ligand–receptor binding kinetics [164, 165, 168]. Extension to an imaging version could extend binding kinetics analyses to whole surfaces. A modality that integrates over a whole image to characterize reversible binding has already been established [169].

Finally, we need to discuss the differences between these schemes and how the data is evaluated. The 2D FCS modalities based on confocal schemes can use the already developed formulas for confocal FCS. This includes not only the parts for diffusion but as well for photophysical and other processes. Here, spatial information can be exploited by calculating spatial cross-correlations. In the case of two observation volumes with negligible cross-talk, the spatial cross-correlation function is given by [170]:

$$G(\tau, d) = \frac{1}{N}\left(1 + \frac{4D\tau}{w_0^2}\right)^{-1}\left(1 + \frac{4D\tau}{z_0^2}\right)^{-\frac{1}{2}} exp\left\{-\frac{d_x^2 + d_y^2}{4D\tau + w_0^2} - \frac{d_z^2}{4D\tau + z_0^2}\right\} \tag{23}$$

Here, d_x, d_y, and d_z are the distances between the two observation volumes in x, y, and z directions, and the other parameters are as previously defined.

As typical in confocal FCS, the observation volume is approximated here by a 3D Gaussian. However, in the case of 2fFCS, this approximation is not sufficient anymore, and a more sophisticated model needs to be used that requires numerical integration [23, 25]. 2fFCS is more robust against typical FCS artefacts, including optical aberrations, e.g., introduced by cover glass thickness variations or mismatch of refractive indices between mounting and immersion medium, and saturation effects stemming from the use of high laser powers for excitation [23, 171]. In the case of TIRF and SPIM-based illuminations with cameras as detectors, the excitation and detection change significantly compared to the confocal case. First, in the confocal case, the excitation profile is a Gaussian function and thus falls off as one moves away from the centre of the focus. In the TIRF and SPIM cases, the excitation intensity is constant in the focal plane and varies only in the axial direction. In addition, while in confocal FCS typically round pinholes are used, pixels on cameras are typically quadratic, which changes and simplifies the derivation of the FCS fit

models [172]. Solutions for single-spot TIRF-FCS correlation functions taking into account the full 3D geometry and also binding interactions are available [166]. In the case of camera-based FCS, assuming measurements in a membrane, i.e., a strictly 2D layer in the focal plane, the correlation function has an analytic solution [173–175]. We provide here the basic correlation function for two square pixels assuming only diffusion and refer the reader to literature for special cases [156]. If we define the function p as

$$p(\tau, d) = \sqrt{\frac{4D\tau + w_0^2}{\pi}} \exp\left\{\frac{d^2}{4D\tau + w_0^2}\right\} + d \times erf\left[\frac{d}{\sqrt{4D\tau + w_0^2}}\right] \tag{24}$$

where d is the distance between two pixels in x- or y-direction, then we can write the function describing the shape of the correlations function separately for the x- and y-directions as

$$g_x(\tau) = (p(\tau,\ a + r_x) + p(\tau,\ a - r_x) - 2p(\tau,\ r_x)) \tag{25}$$

$$g_y(\tau) = \left(p\left(\tau,\ a + r_y\right) + p\left(\tau,\ a - r_y\right) - 2p\left(\tau,\ r_y\right)\right) \tag{26}$$

The function for the 2D case is then just the product of the correlations for the x- and y-directions

$$g(\tau) = g_x(\tau) g_y(\tau) \tag{27}$$

The ACF is obtained by setting the distances r_x and r_y to zero. Finally, we normalize the correlation function with the effective observation volume

$$G(\tau) = \frac{1}{N} \frac{g(\tau)}{g(0)} + G_\infty \tag{28}$$

Normalization ensures that the ACF amplitude is inversely proportional to the number of particles. For the CCF, the peak amplitude is proportional to the particles moving from one pixel to the other. A comparison with the ACFs of the two spatially correlated areas is necessary to deduce the number of cross-correlated particles, similar to dual-colour FCCS. If the two areas to be cross-correlated are not single pixels, then the spatial cross-correlations between two arbitrary binned pixel areas are just the sum of all possible CCFs between all pixels in the two areas [156]. Models for 3D measurements in SPIM-FCS [33, 149, 155] have also been derived, although they neglected cross-talk between pixels. Taking into account cross-talk between pixels, as can be necessary in 3D measurements, requires numerical integration as analytical solutions are no longer obtainable (in preparation).

If the characteristic length scale over which diffusion is measured is precisely known, the methods become essentially calibration-free. In confocal FCS, the precise dimensions of the confocal volume are typically unknown and are alignment

dependent on which FCS is very sensitive. Thus, they need to be calibrated each measurement day. However, Imaging FCS modalities are much less alignment dependent as the illumination intensity is constant, the pixel size and their distance are exactly known, and the microscope PSF of an optical setup, which is an essential determinant of the observation volume of a pixel, typically does not change over time. Thus, Imaging FCS can directly determine the diffusion coefficient (Fig. 8c) without extra calibrations, and D is a fitting parameter in the model. In contrast, in confocal FCS the characteristic time a molecule needs to traverse the confocal observation volume is fitted and later recalculated into diffusion coefficients using a calibration measurement.

However, camera-based methods have also disadvantages. First, they are typically much slower with time resolutions in the millisecond range. This has been addressed by using the newly available SPAD arrays, which can measure faster [21, 22] and can even determine fluorescence lifetimes [129]. In addition, the observation volume in light-sheet microscopy for 3D measurements is generally larger than in the confocal case, limiting the concentration range and the signal-to-noise ratio accessible in SPIM-FCS. This results from the lower numerical aperture of the illumination objectives used in SPIM-FCS, mainly for practical reasons due to space constraints, making it impossible to align two high NA objectives. The lower limit in concentration has been addressed by using two objectives with equal but somewhat lower numerical aperture [176] and by SPIM using a single objective (soSPIM) for illumination, and detection [177]. Finally, the amount of data acquired in any of the 2D FCS methods is typically large as thousands of pixels are recorded over thousands of frames, and thus more storage and faster data evaluation are required. In the last years, several groups have therefore developed GPU based algorithms that speed up data evaluation by 1–2 orders of magnitude [128, 163, 178] and analyse data in real time [179].

5 Concluding Remarks

Correlation-based approaches are compelling tools to extract information from signals by analysing signal fluctuations around their mean value. By using fluorescence as the signal, the measurements become specific and provide single-molecule sensitivity. The resulting Fluorescence Correlation Spectroscopy measurements yield information on molecular transport, actions, and interactions. As FCS was a single-point measurement, it was multiplexed to measure multiple FCS curves simultaneously and was extended to include spatial correlations to obtain more information from a single measurement. We grouped these measurements here under the name of two-dimensional FCS, as they measure some or all points in a 2D sample cross-section and exploit spatial, temporal, or spatiotemporal correlations.

With new developments in microscope, detector, and computational technology and advances in data evaluation strategies, many of these techniques can be now

performed on standard commercially available microscopes without extra modifications. Moreover, the publication of more open-source software tools [179] and reviews around the topic [34, 180] makes two-dimensional FCS easily accessible to a broad spectrum of users (for a list of software, see [175]). Finally, these methods are ideal to be combined with various microscopy and super-resolution techniques [66, 118, 122, 162, 163, 181–184] presenting the possibility to record the structure and dynamics of the system under investigation simultaneously and thus creating a much more complete picture of molecular events in live cells and organisms.

References

1. Magde D, Elson E, Webb WW (1972) Thermodynamic fluctuations in a reacting system – measurement by fluorescence correlation spectroscopy. Phys Rev Lett 29:705–708
2. Ehrenberg M, Rigler R (1974) Rotational Brownian motion and fluorescence intensify fluctuations. Chem Phys 4:390–401
3. Petersen NO, Höddelius PL, Wiseman PW, Seger O, Magnusson KE (1993) Quantitation of membrane receptor distributions by image correlation spectroscopy: concept and application. Biophys J 65:1135–1146
4. Wiseman PW, Brown CM, Webb DJ, Hebert B, Johnson NL, Squier JA, Ellisman MH, Horwitz AF (2004) Spatial mapping of integrin interactions and dynamics during cell migration by image correlation microscopy. J Cell Sci 117:5521–5534
5. Hebert B, Costantino S, Wiseman PW (2005) Spatiotemporal image correlation spectroscopy (STICS) theory, verification, and application to protein velocity mapping in living CHO cells. Biophys J 88:3601–3614
6. Magde D, Webb WW, Elson EL (1978) Fluorescence correlation spectroscopy. III. Uniform translation and laminar flow. Biopolymers 17:361–376
7. Petersen NO (1986) Scanning fluorescence correlation spectroscopy. I. Theory and simulation of aggregation measurements. Biophys J 49:809–815
8. Petersen NO, Johnson DC, Schlesinger MJ (1986) Scanning fluorescence correlation spectroscopy. II. Application to virus glycoprotein aggregation. Biophys J 49:817–820
9. St-Pierre PR, Petersen NO (1990) Relative ligand binding to small or large aggregates measured by scanning correlation spectroscopy. Biophys J 58:503–511
10. St-Pierre PR, Petersen NO (1992) Average density and size of microclusters of epidermal growth factor receptors on A431 cells. Biochemistry 31:2459–2463
11. Pan X, Yu H, Shi X, Korzh V, Wohland T (2007) Characterization of flow direction in microchannels and zebrafish blood vessels by scanning fluorescence correlation spectroscopy. J Biomed Opt 12:1–10
12. Pan X, Shi X, Korzh V, Yu H, Wohland T (2009) Line scan fluorescence correlation spectroscopy for three-dimensional microfluidic flow velocity measurements. J Biomed Opt 14:1–6
13. Koppel DE, Morgan F, Cowan AE, Carson JH (1994) Scanning concentration correlation spectroscopy using the confocal laser microscope. Biophys J 66:502–507
14. Skinner JP, Chen Y, Müller JD (2005) Position-sensitive scanning fluorescence correlation spectroscopy. Biophys J 89:1288–1301
15. Digman MA, Sengupta P, Wiseman PW, Brown CM, Horwitz AR, Gratton E (2005) Fluctuation correlation spectroscopy with a laser-scanning microscope: exploiting the hidden time structure. Biophys J 88:L33–L36
16. Brinkmeier M, Dörre K, Riebeseel K, Rigler R (1997) Confocal spectroscopy in microstructures. Biophys Chem 66:229–239

17. Brinkmeier M, Dörre K, Stephan J, Eigen M (1999) Two-beam cross-correlation: a method to characterize transport phenomena in micrometer-sized structures. Anal Chem 71:609–616
18. Dittrich PS, Schwille P (2002) Spatial two-photon fluorescence cross-correlation spectroscopy for controlling molecular transport in microfluidic structures. Anal Chem 74:4472–4479
19. Jaffiol R, Blancquaert Y, Delon A, Derouard J (2006) Spatial fluorescence cross-correlation spectroscopy. Appl Optics 45:1225–1235
20. Pan X, Foo W, Lim W, Fok MHY, Liu P, Yu H, Maruyama I, Wohland T (2007) Multifunctional fluorescence correlation microscope for intracellular and microfluidic measurements. Rev Sci Instrum 78:53711
21. Scipioni L, Lanzanó L, Diaspro A, Gratton E (2018) Comprehensive correlation analysis for super-resolution dynamic fingerprinting of cellular compartments using the Zeiss Airyscan detector. Nat Commun 9:5120
22. Slenders E, Castello M, Buttafava M, Villa F, Tosi A, Lanzanò L, Koho SV, Vicidomini G (2021) Confocal-based fluorescence fluctuation spectroscopy with a SPAD array detector. Light Sci Appl 10:31
23. Dertinger T, Pacheco V, von der Hocht I, Hartmann R, Gregor I, Enderlein J (2007) Two-focus fluorescence correlation spectroscopy: a new tool for accurate and absolute diffusion measurements. ChemPhysChem 8:433–443
24. Müller CB, Loman A, Richtering W, Enderlein J (2008) Dual-focus fluorescence correlation spectroscopy of colloidal solutions: influence of particle size. J Phys Chem B 112:8236–8240
25. Goossens K, Prior M, Pacheco V, Willbold D, Müllen K, Enderlein J, Hofkens J, Gregor I (2015) Accurate diffusion coefficients of organosoluble reference dyes in organic media measured by dual-focus fluorescence correlation spectroscopy. ACS Nano 9:7360–7373
26. Gösch M, Serov A, Anhut T, Lasser T, Rochas A, Besse PA, Popovic RS, Blom H, Rigler R (2004) Parallel single molecule detection with a fully integrated single-photon 2x2 CMOS detector array. J Biomed Opt 9:913–921
27. Yamamoto J, Mikuni S, Kinjo M (2018) Multipoint fluorescence correlation spectroscopy using spatial light modulator. Biomed Opt Express 9:5881–5890
28. Rochas A, Gosch M, Serov A, Besse PA, Popovic RS, Lasser T, Rigler R (2003) First fully integrated 2-D array of single-photon detectors in standard CMOS technology. IEEE Photon Technol Lett 15:963–965
29. Kannan B, Har JY, Liu P, Maruyama I, Ding JL, Wohland T (2006) Electron multiplying charge-coupled device camera based fluorescence correlation spectroscopy. Anal Chem 78: 3444–3451
30. Burkhardt M, Schwille P (2006) Electron multiplying CCD based detection for spatially resolved fluorescence correlation spectroscopy. Opt Express 14:5013–5020
31. Sisan DR, Arevalo R, Graves C, McAllister R, Urbach JS (2006) Spatially resolved fluorescence correlation spectroscopy using a spinning disk confocal microscope. Biophys J 91: 4241–4252
32. Kannan B, Guo L, Sudhaharan T, Ahmed S, Maruyama I, Wohland T (2007) Spatially resolved total internal reflection fluorescence correlation microscopy using an electron multiplying charge-coupled device camera. Anal Chem 79:4463–4470
33. Singh AP, Krieger JW, Buchholz J, Charbon E, Langowski J, Wohland T (2013) The performance of 2D array detectors for light sheet based fluorescence correlation spectroscopy. Opt Express 21:8652–8668
34. Bag N, Wohland T (2014) Imaging fluorescence fluctuation spectroscopy: new tools for quantitative bioimaging. Annu Rev Phys Chem 65:225–248
35. Singh AP, Wohland T (2014) Applications of imaging fluorescence correlation spectroscopy. Curr Opin Chem Biol 20:29–35
36. Srivastava M, Petersen NO (1996) Image cross-correlation spectroscopy: a new experimental biophysical approach to measurement of slow diffusion of fluorescent molecules. Methods Cell Sci 18:47–54

37. Wiseman PW, Petersen NO (1999) Image correlation spectroscopy. II. Optimization for ultrasensitive detection of preexisting platelet-derived growth factor-beta receptor oligomers on intact cells. Biophys J 76:963–977
38. Costantino S, Comeau JWD, Kolin DL, Wiseman PW (2005) Accuracy and dynamic range of spatial image correlation and cross-correlation spectroscopy. Biophys J 89:1251–1260
39. Rappaz B, Wiseman PW (2013) Image correlation spectroscopy for measurements of particle densities and colocalization. Curr Protoc Cell Biol 59:4.27.1–4.27.15
40. Lajevardipour A, Clayton A (2019) pbICS microscopy technique for determining oligomeric state
41. Comeau JW, Costantino S, Wiseman PW (2006) A guide to accurate fluorescence microscopy colocalization measurements. Biophys J 91:4611–4622
42. Crites TJ, Chen L, Varma R (2022) A TIRF microscopy technique for real-time, simultaneous imaging of the TCR and its associated signaling proteins. J Vis Exp 61:3892
43. Bolte S, Cordelières FP (2006) A guided tour into subcellular colocalization analysis in light microscopy. J Microsc 224:213–232
44. Cerutti E, D'Amico M, Cainero I, Dellino GI, Faretta M, Vicidomini G, Pelicci PG, Bianchini P, Diaspro A, Lanzanò L (2021) Evaluation of sted super-resolution image quality by image correlation spectroscopy (QuICS). Sci Rep 11:20782
45. Oneto M, Scipioni L, Sarmento MJ, Cainero I, Pelicci S, Furia L, Pelicci PG, Dellino GI, Bianchini P, Faretta M, Gratton E, Diaspro A, Lanzanò L (2019) Nanoscale distribution of nuclear sites by super-resolved image cross-correlation spectroscopy. Biophys J 117:2054–2065
46. Cainero I, Cerutti E, Faretta M, Dellino GI, Pelicci PG, Diaspro A, Lanzanò L (2021) Measuring nanoscale distances by structured illumination microscopy and image cross-correlation spectroscopy (SIM-ICCS). Sensors 21
47. Wiseman PW, Squier JA, Ellisman MH, Wilson KR (2000) Two-photon image correlation spectroscopy and image cross-correlation spectroscopy. J Microsc 200:14–25
48. Gopal AA, Rappaz B, Rouger V, Martyn IB, Dahlberg PD, Meland RJ, Beamish IV, Kennedy TE, Wiseman PW (2016) Netrin-1-regulated distribution of UNC5B and DCC in live cells revealed by TICCS. Biophys J 110:623–634
49. Penjweini R, Deville S, Maghsoudi OH, Notelaers K, Ethirajan A, Ameloot M (2019) Investigating the effect of poly-l-lactic acid nanoparticles carrying hypericin on the flow-biased diffusive motion of HeLa cell organelles. J Pharm Pharmacol 71:104–116
50. Kolin DL, Wiseman PW (2007) Advances in image correlation spectroscopy: measuring number densities, aggregation states, and dynamics of fluorescently labeled macromolecules in cells. Cell Biochem Biophys 49:141–164
51. Petersen NO, Brown C, Kaminski A, Rocheleau J, Srivastava M, Wiseman PW (1998) Analysis of membrane protein cluster densities and sizes in situ by image correlation spectroscopy. Faraday Discuss 111:289–243
52. Mets RD, Wang I, Balland M, Oddou C, Moreau P, Fourcade B, Albiges-Rizo C, Delon A, Destaing O (2019) Cellular tension encodes local Src-dependent differential β 1 and β 3 integrin mobility. Mol Biol Cell 30:181–190
53. Altmann SM, Lenne PF (2002) Forced unfolding of single proteins. Methods Cell Biol 68: 311–335
54. Nayal A, Webb DJ, Brown CM, Schaefer EM, Vicente-Manzanares M, Horwitz AR (2006) Paxillin phosphorylation at Ser273 localizes a GIT1–PIX–PAK complex and regulates adhesion and protrusion dynamics. J Cell Biol 173:587–589
55. Travagliati M, Girardo S, Pisignano D, Beltram F, Cecchini M (2013) Easy monitoring of velocity fields in microfluidic devices using spatiotemporal image correlation spectroscopy. Anal Chem 85:8080–8084
56. Coppola S, Pozzi D, Sanctis SCD, Digman MA, Gratton E, Caracciolo G (2013) Quantitative measurement of intracellular transport of nanocarriers by spatio-temporal image correlation spectroscopy. Methods Appl Fluoresc 1:15005

57. Potvin-Trottier L, Lord ND, Vinnicombe G, Paulsson J (2016) Synchronous long-term oscillations in a synthetic gene circuit. Nature 538:514–517
58. Harrison PL, Heath GR, Johnson BRG, Abdel-Rahman MA, Strong PN, Evans SD, Miller K (2016) Phospholipid dependent mechanism of smp24, an α-helical antimicrobial peptide from scorpion venom. Biochim Biophys Acta 1858:2737–2744
59. Nie J, Xu C, Jin J, Aka JA, Tempel W, Nguyen V, You L, Weist R, Min J, Pawson T, Yang XJ (2015) Ankyrin repeats of ANKRA2 recognize a PxLPxL motif on the 3M syndrome protein CCDC8. Structure 23:700–712
60. Rowland DJ, Tuson HH, Biteen JS (2016) Resolving fast, confined diffusion in bacteria with image correlation spectroscopy. Biophys J 110:2241–2251
61. Petrášek Z, Hoege C, Hyman AA, Schwille P (2008) Two-photon fluorescence imaging and correlation analysis applied to protein dynamics in C. elegans embryo
62. Pandžić E, Rossy J, Gaus K (2015) Tracking molecular dynamics without tracking: image correlation of photo-activation microscopy. Methods Appl Fluoresc 3:14006
63. Toplak T, Pandzic E, Chen L, Vicente-Manzanares M, Horwitz AR, Wiseman PW (2012) STICCS reveals matrix-dependent adhesion slipping and gripping in migrating cells. Biophys J 103:1672–1682
64. Semrau S, Schmidt T (2007) Particle image correlation spectroscopy (PICS): retrieving nanometer-scale correlations from high-density single-molecule position data. Biophys J 92: 613–621
65. Dupont A, Stirnnagel K, Lindemann D, Lamb DC (2013) Tracking image correlation: combining single-particle tracking and image correlation. Biophys J 104:2373–2382
66. Ashdown G, Cope A, Wiseman P, Owen D (2014) Molecular flow quantified beyond the diffraction limit by spatiotemporal image correlation of structured illumination microscopy data. Biophys J 107:L21–L23
67. Kolin DL, Ronis D, Wiseman PW (2006) k-Space image correlation spectroscopy: a method for accurate transport measurements independent of fluorophore photophysics. Biophys J 91: 3061–3075
68. Waithe D, Brown JM, Reglinski K, Diez-Sevilla I, Roberts D, Eggeling C (2020) Object detection networks and augmented reality for cellular detection in fluorescence microscopy. J Cell Biol 219:e201903166
69. Kolin DL, Costantino S, Wiseman PW (2006) Sampling effects, noise, and photobleaching in temporal image correlation spectroscopy. Biophys J 90:628–639
70. Bouzin M, Sironi L, Chirico G, D'Alfonso L, Inverso D, Pallavicini P, Collini M (2015) An intermittent model for intracellular motions of gold nanostars by k-space scattering image correlation. Biophys J 109:2246–2258
71. Brandão HB, Sangji H, Pandžić E, Bechstedt S, Brouhard GJ, Wiseman PW (2014) Measuring ligand–receptor binding kinetics and dynamics using k-space image correlation spectroscopy. Methods 66:273–282
72. Kure JL, Andersen CB, Mortensen KI, Wiseman PW, Arnspang EC (2020) Revealing plasma membrane nano-domains with diffusion analysis methods. Membranes 10:314
73. Arnspang EC, Schwartzentruber J, Clausen MP, Wiseman PW, Lagerholm BC (2013) Bridging the gap between single molecule and ensemble methods for measuring lateral dynamics in the plasma membrane. PLoS One 8:e78096
74. Arnspang EC, Login FH, Koffman JS, Sengupta P, Nejsum LN (2016) AQP2 plasma membrane diffusion is altered by the degree of AQP2-S256 phosphorylation. Int J Mol Sci 17:1804
75. Di Rienzo C, Gratton E, Beltram F, Cardarelli F (2013) Fast spatiotemporal correlation spectroscopy to determine protein lateral diffusion laws in live cell membranes. Proc Natl Acad Sci 110:12307
76. Di Rienzo C, Piazza V, Gratton E, Beltram F, Cardarelli F (2014) Probing short-range protein Brownian motion in the cytoplasm of living cells. Nat Commun 5:5891

77. Digiacomo L, Digman MA, Gratton E, Caracciolo G (2016) Development of an image mean square displacement (iMSD)-based method as a novel approach to study the intracellular trafficking of nanoparticles. Acta Biomater 42:189–198
78. Di Rienzo C, Cardarelli F, Di Luca M, Beltram F, Gratton E (2016) Diffusion tensor analysis by two-dimensional pair correlation of fluorescence fluctuations in cells. Biophys J 111:841–851
79. Wawrezinieck L, Rigneault H, Marguet D, Lenne P-F (2005) Fluorescence correlation spectroscopy diffusion laws to probe the submicron cell membrane organization. Biophys J 89: 4029–4042
80. Masuda A, Ushida K, Okamoto T (2005) New fluorescence correlation spectroscopy enabling direct observation of spatiotemporal dependence of diffusion constants as an evidence of anomalous transport in extracellular matrices. Biophys J 88:3584–3591
81. Hendrix J, Baumgärtel V, Schrimpf W, Ivanchenko S, Digman MA, Gratton E, Kräusslich H-G, Müller B, Lamb DC (2015) Live-cell observation of cytosolic HIV-1 assembly onset reveals RNA-interacting Gag oligomers. J Cell Biol 210:629–646
82. Digman MA, Gratton E (2009) Imaging barriers to diffusion by pair correlation functions. Biophys J 97:665–673
83. Cardarelli F, Gratton E (2010) In vivo imaging of single-molecule translocation through nuclear pore complexes by pair correlation functions. PLoS One 5:e10475
84. Hinde E, Cardarelli F, Digman MA, Gratton E (2010) In vivo pair correlation analysis of EGFP intranuclear diffusion reveals DNA-dependent molecular flow. Proc Natl Acad Sci 107: 16560
85. Hinde E, Cardarelli F, Digman MA, Kershner A, Kimble J, Gratton E (2011) The impact of mitotic versus interphase chromatin architecture on the molecular flow of EGFP by pair correlation analysis. Biophys J 100:1829–1836
86. Hinde E, Kong X, Yokomori K, Gratton E (2014) Chromatin dynamics during DNA repair revealed by pair correlation analysis of molecular flow in the nucleus. Biophys J 107:55–65
87. Baum M, Erdel F, Wachsmuth M, Rippe K (2014) Retrieving the intracellular topology from multi-scale protein mobility mapping in living cells. Nat Commun 5:4494
88. Niklas P, Elina S, Bagawath S, Sofia J, Enrico G (2019) Pair correlation analysis maps the dynamic two-dimensional organization of natural killer cell receptors at the synapse. ACS Nano 13:14274–14282
89. Clark NM, Hinde E, Winter CM, Fisher AP, Crosti G, Blilou I, Gratton E, Benfey PN, Sozzani R (2016) Tracking transcription factor mobility and interaction in arabidopsis roots with fluorescence correlation spectroscopy. Elife 5:e14770
90. Sengupta P, Jovanovic-Talisman T, Skoko D, Renz M, Veatch SL, Lippincott-Schwartz J (2011) Probing protein heterogeneity in the plasma membrane using PALM and pair correlation analysis. Nat Methods 8:969–975
91. Koltermann A, Kettling U, Bieschke J, Winkler T, Eigen M (1998) Rapid assay processing by integration of dual-color fluorescence cross-correlation spectroscopy: high throughput screening for enzyme activity. Proc Natl Acad Sci 95:1421
92. Bieschke J, Giese A, Schulz-Schaeffer W, Zerr I, Poser S, Eigen M, Kretzschmar H (2000) Ultrasensitive detection of pathological prion protein aggregates by dual-color scanning for intensely fluorescent targets. Proc Natl Acad Sci 97:5468
93. Weissman M, Schindler H, Feher G (1976) Determination of molecular weights by fluctuation spectroscopy: application to DNA. Proc Natl Acad Sci U S A 73:2776–2780
94. Koppel DE (1974) Statistical accuracy in fluorescence correlation spectroscopy. Phys Rev A 10:1938–1945
95. Unruh JR, Gratton E (2008) Analysis of molecular concentration and brightness from fluorescence fluctuation data with an electron multiplied CCD camera. Biophys J 95:5385–5398
96. Xia KQ, Xin YB, Tong P (1995) Dual-beam incoherent cross-correlation spectroscopy. J Opt Soc Am A 12:1571–1578

97. Cardarelli F, Lanzano L, Gratton E (2011) Fluorescence correlation spectroscopy of intact nuclear pore complexes. Biophys J 101:L27–L29
98. Cardarelli F, Lanzano L, Gratton E (2012) Capturing directed molecular motion in the nuclear pore complex of live cells. Proc Natl Acad Sci 109:9863
99. Ruan Q, Cheng MA, Levi M, Gratton E, Mantulin WW (2004) Spatial-temporal studies of membrane dynamics: scanning fluorescence correlation spectroscopy (SFCS). Biophys J 87: 1260–1267
100. Petrásek Z, Schwille P (2008) Precise measurement of diffusion coefficients using scanning fluorescence correlation spectroscopy. Biophys J 94:1437–1448
101. Petrášek Z, Derenko S, Schwille P (2011) Circular scanning fluorescence correlation spectroscopy on membranes. Opt Express 19:25006–25021
102. Waithe D, Schneider F, Chojnacki J, Clausen MP, Shrestha D, de la Serna JB, Eggeling C (2018) Optimized processing and analysis of conventional confocal microscopy generated scanning FCS data. Methods 140–141:62
103. Bona MD, Mancini MA, Mazza D, Vicidomini G, Diaspro A, Lanzanò L (2019) Measuring mobility in chromatin by intensity-sorted FCS. Biophys J 116:987–999
104. Ries J, Schwille P (2006) Studying slow membrane dynamics with continuous wave scanning fluorescence correlation spectroscopy. Biophys J 91:1915–1924
105. García-Sáez AJ, Carrer DC, Schwille P (2010) Fluorescence correlation spectroscopy for the study of membrane dynamics and organization in giant unilamellar vesicles. Methods Mol Biol 606:493–508
106. Eckert AF, Gao P, Wesslowski J, Wang X, Rath J, Nienhaus K, Davidson G, Nienhaus GU (2020) Measuring ligand-cell surface receptor affinities with axial line-scanning fluorescence correlation spectroscopy. Elife 9:e55286
107. Chiantia S, Ries J, Kahya N, Schwille P (2006) Cover picture: combined AFM and two-focus SFCS study of raft-exhibiting model membranes (ChemPhysChem 11/2006). ChemPhysChem 7:2229–2229
108. Ries J, Yu SR, Burkhardt M, Brand M, Schwille P (2009) Modular scanning FCS quantifies receptor-ligand interactions in living multicellular organisms. Nat Methods 6:643–645
109. Gao P, Nienhaus GU (2021) Axial line-scanning stimulated emission depletion fluorescence correlation spectroscopy. Opt Lett 46:2184–2187
110. Dörlich RM, Chen Q, Hedde PN, Schuster V, Hippler M, Wesslowski J, Davidson G, Nienhaus GU (2015) Dual-color dual-focus line-scanning FCS for quantitative analysis of receptor-ligand interactions in living specimens. Sci Rep 5:10149
111. Rossow MJ, Sasaki JM, Digman MA, Gratton E (2010) Raster image correlation spectroscopy in live cells. Nat Protoc 5:1761–1774
112. Digman MA, Gratton E (2009) Analysis of diffusion and binding in cells using the RICS approach. Microsc Res Tech 72:323–332
113. Digman MA, Wiseman PW, Horwitz AR, Gratton E (2009) Detecting protein complexes in living cells from laser scanning confocal image sequences by the cross correlation raster image spectroscopy method. Biophys J 96:707–716
114. Sasaki A, Yamamoto J, Jin T, Kinjo M (2015) Raster image cross-correlation analysis for spatiotemporal visualization of intracellular degradation activities against exogenous DNAs. Sci Rep 5:14428
115. Hendrix J, Dekens T, Schrimpf W, Lamb D (2016) Arbitrary-region raster image correlation spectroscopy. Biophys J 111:1785–1796
116. Mikuni S, Yamamoto J, Horio T, Kinjo M (2017) Negative correlation between the diffusion coefficient and transcriptional activity of the glucocorticoid receptor. Int J Mol Sci 18
117. Scipioni L, Di Bona M, Vicidomini G, Diaspro A, Lanzanò L (2018) Local raster image correlation spectroscopy generates high-resolution intracellular diffusion maps. Commun Biol 1:10
118. Eggeling C, Ringemann C, Medda R, Schwarzmann G, Sandhoff K, Polyakova S, Belov VN, Hein B, Middendorff CV, Schönle A, Hell SW (2009) Direct observation of the nanoscale dynamics of membrane lipids in a living cell. Nature 457:1159–1162

119. Hedde PN, Dörlich RM, Blomley R, Gradl D, Oppong E, Cato ACB, Nienhaus GU (2013) Stimulated emission depletion-based raster image correlation spectroscopy reveals biomolecular dynamics in live cells. Nat Commun 4:2093
120. Longfils M, Smisdom N, Ameloot M, Rudemo M, Lemmens V, Fernández GS, Röding M, Lorén N, Hendrix J, Särkkä A (2019) Raster image correlation spectroscopy performance evaluation. Biophys J 117:1900–1914
121. Norris SCP, Humpolíčková J, Amler E, Huranová M, Buzgo M, Macháň R, Lukáš D, Hof M (2011) Raster image correlation spectroscopy as a novel tool to study interactions of macromolecules with nanofiber scaffolds. Acta Biomater 7:4195–4203
122. Honigmann A, Mueller V, Ta H, Schoenle A, Sezgin E, Hell SW, Eggeling C (2014) Scanning STED-FCS reveals spatiotemporal heterogeneity of lipid interaction in the plasma membrane of living cells. Nat Commun 5:5412
123. Honigmann A, Sadeghi S, Keller J, Hell SW, Eggeling C, Vink R (2014) A lipid bound actin meshwork organizes liquid phase separation in model membranes. Elife 3:e01671
124. Benda A, Ma Y, Gaus K (2015) Self-calibrated line-scan STED-FCS to quantify lipid dynamics in model and cell membranes. Biophys J 108:596–609
125. Moens PDJ, Digman MA, Gratton E (2015) Modes of diffusion of cholera toxin bound to GM1 on live cell membrane by image mean square displacement analysis. Biophys J 108: 1448–1458
126. Needleman DJ, Xu Y, Mitchison TJ (2009) Pin-hole array correlation imaging: highly parallel fluorescence correlation spectroscopy. Biophys J 96:5050–5059
127. Vitali M, Bronzi D, Krmpot AJ, Nikolić SN, Schmitt FJ, Junghans C, Tisa S, Friedrich T, Vukojević V, Terenius L, Zappa F, Rigler R (2014) A single-photon avalanche camera for fluorescence lifetime imaging microscopy and correlation spectroscopy. IEEE J Sel Top Quantum Electron 20:344–353
128. Krmpot AJ, Nikolić SN, Oasa S, Papadopoulos DK, Vitali M, Oura M, Mikuni S, Thyberg P, Tisa S, Kinjo M, Nilsson L, Terenius L, Rigler R, Vukojević V (2019) Functional fluorescence microscopy imaging: quantitative scanning-free confocal fluorescence microscopy for the characterization of fast dynamic processes in live cells. Anal Chem 91:11129–11137
129. Oasa S, Krmpot AJ, Nikolić SN, Clayton AHA, Tsigelny IF, Changeux J-P, Terenius L, Rigler R, Vukojević V (2021) Dynamic cellular cartography: mapping the local determinants of oligodendrocyte transcription factor 2 (OLIG2) function in live cells using massively parallel fluorescence correlation spectroscopy integrated with fluorescence lifetime imaging microscopy (mpFCS/FLIM). Anal Chem 93:12011–12021
130. Toomre D, Pawley JB (2006) Disk-scanning confocal microscopy. Springer, Boston, pp 221–238
131. Ohsugi Y, Kinjo M (2009) Multipoint fluorescence correlation spectroscopy with total internal reflection fluorescence microscope. J Biomed Opt 14:14030
132. Wohland T, Shi X, Sankaran J, Stelzer EHK (2010) Single plane illumination fluorescence correlation spectroscopy (SPIM-FCS) probes inhomogeneous three-dimensional environments. Opt Express 18:10627–10641
133. Struntz P, Weiss M (2015) Multiplexed measurement of protein diffusion in Caenorhabditis elegans embryos with SPIM-FCS. J Phys D Appl Phys 49:44002
134. Bag N, Sankaran J, Paul A, Kraut RS, Wohland T (2012) Calibration and limits of camera-based fluorescence correlation spectroscopy: a supported lipid bilayer study. ChemPhysChem 13:2784–2794
135. Harwardt M-LIE, Dietz MS, Heilemann M, Wohland T (2018) SPT and imaging FCS provide complementary information on the dynamics of plasma membrane molecules. Biophys J 114: 2432–2443
136. Macháň R, Foo YH, Wohland T (2016) On the equivalence of FCS and FRAP: simultaneous lipid membrane measurements. Biophys J 111:152–161
137. Gupta A, Phang IY, Wohland T (2020) To hop or not to hop: exceptions in the FCS diffusion law. Biophys J 118:2434–2447

138. Cooper JT, Peterson EM, Harris JM (2013) Fluorescence imaging of single-molecule retention trajectories in reversed-phase chromatographic particles. Anal Chem 85:9363–9370
139. Xu H, Nagasaka S, Kameta N, Masuda M, Ito T, Higgins DA (2016) Imaging fluorescence correlation spectroscopy studies of dye diffusion in self-assembled organic nanotubes. Phys Chem Chem Phys 18:16766–16774
140. Erstling JA, Hinckley JA, Bag N, Hersh J, Feuer GB, Lee R, Malarkey HF, Yu F, Ma K, Baird BA, Wiesner UB (2021) Ultrasmall, bright, and photostable fluorescent core–shell aluminosilicate nanoparticles for live-cell optical super-resolution microscopy. Adv Mater 33:2006829
141. Bag N, Yap DHX, Wohland T (2014) Temperature dependence of diffusion in model and live cell membranes characterized by imaging fluorescence correlation spectroscopy. Biochim Biophys Acta 1838:802–813
142. Gupta A, Marzinek JK, Jefferies D, Bond PJ, Harryson P, Wohland T (2019) The disordered plant dehydrin Lti30 protects the membrane during water-related stress by cross-linking lipids. J Biol Chem 294:6468–6482
143. Bag N, Ali A, Chauhan VS, Wohland T, Mishra A (2013) Membrane destabilization by monomeric hIAPP observed by imaging fluorescence correlation spectroscopy. Chem Commun 49:9155–9157
144. Bag N, Huang S, Wohland T (2015) Plasma membrane organization of epidermal growth factor receptor in resting and ligand-bound states. Biophys J 109:1925–1936
145. Bag N, Ng XW, Sankaran J, Wohland T (2016) Spatiotemporal mapping of diffusion dynamics and organization in plasma membranes. Methods Appl Fluoresc 4:34003
146. Azbazdar Y, Ozalp O, Sezgin E, Veerapathiran S, Duncan AL, Sansom MSP, Eggeling C, Wohland T, Karaca E, Ozhan G (2019) More favorable palmitic acid over palmitoleic acid modification of Wnt3 ensures its localization and activity in plasma membrane domains. Front Cell Dev Biol 7:281
147. Bag N, Holowka DA, Baird BA (2020) Imaging FCS delineates subtle heterogeneity in plasma membranes of resting mast cells. Mol Biol Cell 31:709–723
148. Bag N, Wagenknecht-Wiesner A, Lee A, Shi SM, Holowka DA, Baird BA (2021) Lipid-based and protein-based interactions synergize transmembrane signaling stimulated by antigen clustering of IgE receptors. Proc Natl Acad Sci 118:e2026583118
149. Krieger JW, Singh AP, Bag N, Garbe CS, Saunders TE, Langowski J, Wohland T (2015) Imaging fluorescence (cross-) correlation spectroscopy in live cells and organisms. Nat Protoc 10:1948–1974
150. Ng X, Teh C, Korzh V, Wohland T (2016) The secreted signaling protein Wnt3 is associated with membrane domains in vivo: a SPIM-FCS study. Biophys J 111:418–429
151. Dhasmana D, Veerapathiran S, Azbazdar Y, Nelanuthala AVS, Teh C, Ozhan G, Wohland T (2021) Wnt3 is lipidated at conserved cysteine and serine residues in zebrafish neural tissue. Front Cell Dev Biol 9:671218
152. Sankaran J, Tan NJHJ, But KP, Cohen Y, Rice SA, Wohland T (2019) Single microcolony diffusion analysis in Pseudomonas aeruginosa biofilms. NPJ Biofilms Microbiomes 5:35
153. Pernuš A, Langowski J (2015) Imaging Fos-Jun transcription factor mobility and interaction in live cells by single plane illumination-fluorescence cross correlation spectroscopy. PLoS One 10:e0123070
154. Yavas S, Macháň R, Wohland T (2016) The epidermal growth factor receptor forms location-dependent complexes in resting cells. Biophys J 111:2241–2254
155. Krieger JW, Singh AP, Garbe CS, Wohland T, Langowski J (2014) Dual-color fluorescence cross-correlation spectroscopy on a single plane illumination microscope (SPIM-FCCS). Opt Express 22:2358–2375
156. Sankaran J, Manna M, Guo L, Kraut R, Wohland T (2009) Diffusion, transport, and cell membrane organization investigated by imaging fluorescence cross-correlation spectroscopy. Biophys J 97:2630–2639
157. Lenne P-F, Wawrezinieck L, Conchonaud F, Wurtz O, Boned A, Guo X-J, Rigneault H, He H-T, Marguet D (2006) Dynamic molecular confinement in the plasma membrane by microdomains and the cytoskeleton meshwork. EMBO J 25:3245–3256

158. Favard C, Wenger J, Lenne PF, Rigneault H (2011) FCS diffusion laws in two-phase lipid membranes: determination of domain mean size by experiments and Monte Carlo simulations. Biophys J 100:1242–1251
159. Huang H, Simsek MF, Jin W, Pralle A (2015) Effect of receptor dimerization on membrane lipid raft structure continuously quantified on single cells by camera based fluorescence correlation spectroscopy. PLoS One 10:e0121777
160. Ng XW, Bag N, Wohland T (2015) Characterization of lipid and cell membrane organization by the fluorescence correlation spectroscopy diffusion law. CHIMIA Int J Chem 69:112–119
161. Veerapathiran S, Wohland T (2018) The imaging FCS diffusion law in the presence of multiple diffusive modes. Methods 140:140–150
162. Kisley L, Brunetti R, Tauzin LJ, Shuang B, Yi X, Kirkeminde AW, Higgins DA, Weiss S, Landes CF (2015) Characterization of porous materials by fluorescence correlation spectroscopy super-resolution optical fluctuation imaging. ACS Nano 9:9158–9166
163. Sankaran J, Balasubramanian H, Tang WH, Ng XW, Röllin A, Wohland T (2021) Simultaneous spatiotemporal super-resolution and multi-parametric fluorescence microscopy. Nat Commun 12:1748
164. Thompson NL, Burghardt TP, Axelrod D (1981) Measuring surface dynamics of biomolecules by total internal reflection fluorescence with photobleaching recovery or correlation spectroscopy. Biophys J 33:435–454
165. Thompson NL, Axelrod D (1983) Immunoglobulin surface-binding kinetics studied by total internal reflection with fluorescence correlation spectroscopy. Biophys J 43:103–114
166. Hassler K, Anhut T, Rigler R, Gösch M, Lasser T (2005) High count rates with total internal reflection fluorescence correlation spectroscopy. Biophys J 88:L01–L03
167. Hassler K, Leutenegger M, Rigler P, Rao R, Rigler R, Gösch M, Lasser T (2005) Total internal reflection fluorescence correlation spectroscopy (TIR-FCS) with low background and high count-rate per molecule. Opt Express 13:7415–7423
168. Thompson NL, Steele BL (2007) Total internal reflection with fluorescence correlation spectroscopy. Nat Protoc 2:878–890
169. Mücksch J, Blumhardt P, Strauss MT, Petrov EP, Jungmann R, Schwille P (2018) Quantifying reversible surface binding via surface-integrated fluorescence correlation spectroscopy. Nano Lett 18:3185–3192
170. Weidemann T, Wachsmuth M, Tewes M, Rippe K, Langowski J (2002) Analysis of ligand binding by two-colour fluorescence cross-correlation spectroscopy. Single Mol 3:49–61
171. Müller CB, Loman A, Pacheco V, Koberling F, Willbold D, Richtering W, Enderlein J (2008) Precise measurement of diffusion by multi-color dual-focus fluorescence correlation spectroscopy. Europhys Lett 83:46001
172. Ries J, Petrov EP, Schwille P (2008) Total internal reflection fluorescence correlation spectroscopy: effects of lateral diffusion and surface-generated fluorescence. Biophys J 95: 390–399
173. Sankaran J, Bag N, Kraut RS, Wohland T (2013) Accuracy and precision in camera-based fluorescence correlation spectroscopy measurements. Anal Chem 85:3948–3954
174. Sankaran J, Shi X, Ho LY, Stelzer EH, Wohland T (2010) ImFCS: a software for imaging FCS data analysis and visualization. Opt Express 18:25468–25481
175. Wohland T, Maiti S, Macháň R (2020) An introduction to fluorescence correlation spectroscopy
176. Capoulade J, Wachsmuth M, Hufnagel L, Knop M (2011) Quantitative fluorescence imaging of protein diffusion and interaction in living cells. Nat Biotechnol 29:835–839
177. Singh AP, Galland R, Finch-Edmondson ML, Grenci G, Sibarita JB, Studer V, Viasnoff V, Saunders TE (2017) 3D protein dynamics in the cell nucleus. Biophys J 112:133–142
178. Yoshida S, Schmid W, Vo N, Calabrase W, Kisley L (2021) Computationally-efficient spatiotemporal correlation analysis super-resolves anomalous diffusion. Opt Express 29: 7616–7629

179. Aik DYK, Wohland T (2022) Microscope alignment using real-time imaging FCS. Biophys J 121:2663–2670
180. Yu L, Lei Y, Ma Y, Liu M, Zheng J, Dan D, Gao P (2021) A comprehensive review of fluorescence correlation spectroscopy. Front Physiol 9:644450
181. Leutenegger M, Ringemann C, Lasser T, Hell SW, Eggeling C (2012) Fluorescence correlation spectroscopy with a total internal reflection fluorescence STED microscope (TIRF-STED-FCS). Opt Express 20:5243–5263
182. Ashdown GW, Burn GL, Williamson DJ, Pandžić E, Peters R, Holden M, Ewers H, Shao L, Wiseman PW, Owen DM (2017) Live-cell super-resolution reveals F-actin and plasma membrane dynamics at the T cell synapse. Biophys J 112:1703–1713
183. Ashdown GW, Owen DM (2018) Spatio-temporal image correlation spectroscopy and super-resolution microscopy to quantify molecular dynamics in T cells. Methods 140–141:112–118
184. Schnitzbauer J, Wang Y, Zhao S, Bakalar M, Nuwal T, Chen B, Huang B (2018) Correlation analysis framework for localization-based superresolution microscopy. Proc Natl Acad Sci 115:3219